Kobe University Repository : Kernel

PDF issue: 2024-11-05

Quantitative analysis of the oocyte quality changes and the fertilization Ca^{2+} wave in C. elegans

Imakubo, Momoko

(Degree)
博士（工学）
(Date of Degree)
2021-03-25
(Date of Publication)
2023-03-25
(Resource Type)
doctoral thesis
(Report Number)
甲第8076号
(URL)
https://hdl.handle.net/20.500.14094/D1008076

※ 当コンテンツは神戸大学の学術成果です。無断複製・不正使用等を禁じます。著作権法で認められている範囲内で、適切にご利用ください。

Doctoral Dissertation

Quantitative analysis of the oocyte quality changes and the fertilization Ca^{2+} wave in *C. elegans*

線虫 *C. elegans* の卵母細胞の質的変化および受精カルシウム波についての数理解析

Momoko Imakubo

今久保　桃子

January 2021

Graduate School of System Informatics, Kobe University

Abstract

Oocytes acquire the ability to support fertilization and development during meiotic maturation through processes, such as the breakdown of the germinal vesicle, chromosome condensation, spindle formation, and accumulation of mRNA and protein required for development. The fertilization and developmental ability of oocytes affects not only fertilization and early embryonic development but also the establishment and maintenance of pregnancy and fetal development. However, the mechanisms of phenomena in oocytes related to fertilization and developmental ability remain poorly understood.

Oocyte quality is an important factor for success of embryonic development. The fertilization and developmental ability of oocytes, referred to as oocyte quality, decreases with increasing maternal age. A decline in female reproduction is one of the earliest hallmarks of aging, which increases the risk of infertility, birth defects, and miscarriage. Age-related decreases in oocyte quality are thought to cause infertility in many animals, including invertebrates and mammals. However, the mechanisms of the age-related decreases in oocyte quality have not yet been fully understood.

The Ca^{2+} waves occur during fertilization in almost all animal species and trigger the oocyte activation. Oocytes arrested in meiosis are activated by propagation of intracellular Ca^{2+} waves at fertilization. The Ca^{2+} waves trigger multi-faceted cellular processes, including resumption of meiosis, cortical granule exocytosis, and formation of the pronucleus, which are required for embryo development. Although the fertilization Ca^{2+} waves are key process for fertilization and embryo development, mechanisms underlying the generation of Ca^{2+} waves have not been fully elucidated.

This dissertation focuses on the age-related changes in oocyte quality and the fertilization Ca^{2+} waves as universal and important phenomena for fertilization and development. While there are many studies that analyzed the phenomena based on biological experimental approaches, few studies quantitatively and mathematically analyzed them based on informatics approaches. Quantitative and mathematical analyses are expected to provide new biological findings that are different from those derived from biological experimental approaches. The purpose of this study is to provide new findings and insights regarding the age-related changes in oocyte quality and the fertilization Ca^{2+} waves. I performed image processing and mathematical modeling of in vivo imaging data of oocytes in the nematode *Caenorhabditis elegans* (*C. elegans*) as a model organism.

Firstly, to quantify the age-related changes in oocyte quality, I proposed statistical image features to characterize the changes in the appearance of *C. elegans* oocytes with aging using images captured by Nomarski differential interference contrast (DIC) microscopy. I showed that the cytoplasmic texture significantly changes with aging through the statistical image features of Max-min Value (Mm Value) and *Correlation* (COR); the Mm Value is defined as the mean

difference between the maximum and minimum intensities within each moving window and COR is the Grey Level Co-occurrence Matrix based feature. The analyses using synthetic images with changing the granule size suggest that the texture changes characterized by COR reflect an increasing of the granule size in the cytoplasm. Furthermore, manual measurements of the granule size in DIC images validated that the granule size increases with aging. The relationship between granule size and fertility is expected to be elucidated by future biological experiments in this and other species.

Secondly, I predicted the genes involved in reproductive aging by applying the proposed statistical texture analysis methods to DIC microscopy images of early *C. elegans* embryos from large-scale gene silencing experiments. Genes that cause the similar texture changes as seen in aged oocytes are candidate genes involved in the reproductive aging. These candidate genes were identified by their images that had a decreased Mm Value or increased COR – properties that were found to occur in aged oocytes. Of the 316 genes tested, five genes (*smc-4*, F10C2.4, *tin-44*, *let-754*, *hmp-2*) were identified to decrease Mm Values and one gene (*csr-1*) was identified to increase COR. The candidate genes included genes related to age-related function, such as chromosome segregation (*smc-4*, F10C2.4) and mitochondrial function (*tin-44*) and some genes that are not known to be related to aging (*let-754*, *hmp-2*). Of the identified genes, *smc-4*, which has functions related to chromosome segregation, is known to be involved in the reproductive aging of *C. elegans*. These results suggest that the screening using the image features enable to predict genes involved in reproductive aging. Through these analyses, the candidate genes were identified to potentially be involved in reproductive aging. The involvement of the candidate genes in reproductive aging is expected to be confirmed by future biological experiments.

Finally, to understand the mechanisms of generating fertilization Ca^{2+} waves, I proposed a mathematical model of the fertilization Ca^{2+} wave in *C. elegans*. The reaction-diffusion Nagumo model, which was previously proposed to model the Ca^{2+}-induced Ca^{2+}-release mechanism, reproduces the biphasic nature of the Ca^{2+} wave observed in the experiment. However, the previous model could not represent the gradient of the convergence concentration depending on the distance from the fertilization point. To propose the model that satisfies both conditions of formation of a biphasic wave and the gradual decrease of the convergence concentration depending on the position, I modified the Nagumo model by introducing a linear monotonically decreasing function into the reaction part. I demonstrated that my new model can produce the Ca^{2+} wave form that satisfied both conditions simultaneously. The proposed model suggests spatial non-uniformity in the amounts of Ca^{2+} released from cytoplasm during fertilization. I hope that the existence of spatial non-uniformity will be confirmed by future experimental studies. Gradual decrease of Ca^{2+} concentration after convergence, which was observed in vivo, cannot be represented by the proposed model. Our model needs improvement in the future. Extension to three-dimensional simulations is also expected in the future.

I quantitatively and mathematically analyzed the age-related changes in oocyte quality and the fertilization Ca^{2+} wave, which are important phenomena related to fertilization and developmental ability of oocytes. I have derived new

findings and insights that are potentially useful for understanding phenomena related to the fertilization and developmental ability of oocytes.

Contents

Abbreviations

ART	assisted reproductive technology
CICR	Ca^{2+}-induced Ca^{2+}-release
COR	*Correlation*
DIC	differential interference contrast
GLCM	Gray Level Co-occurrence Matrix
ICSI	intracytoplasmic sperm injection
IP3	inositol 1, 4, 5-trisphosphate
Mm Value	Max-min Value
RNAi	RNA interference
ROI	region of interest
WDDD	Worm Developmental Dynamics Database

Chapter 1

Introduction

1.1 Research Background

Animal development begins with a single fertilized egg. The fertilized egg undergoes cell divisions and cells differentiate into the organs and the fully formed multicellular organism. In sexual reproduction, fertilization is the process in which gametes fuse to form a zygote. Gametes, i.e., sperm and oocytes are generated through a specialized cell division process, called meiosis, which consists a single round of DNA replication and two cell divisions. The process of meiosis greatly differs between sperm and oocytes. Sperm are formed without interruption of meiosis, whereas oocytes arrest at prophase of meiosis I in most animal species [1][2]. In response to a hormonal stimulus, oocytes undergo meiotic maturation, including breakdown of the germinal vesicle, chromosome condensation, and spindle formation [2][3].

The ability of the oocytes to support fertilization, embryonic development, and full-term development is called developmental competence or oocyte quality [4]. Oocyte quality affects not only fertilization and early embryonic development but also the establishment and maintenance of pregnancy and fetal development [5]. It is widely known that advanced maternal age decreases oocyte quality. As woman aging, quantity and quality of oocytes decrease gradually, which increase risk of infertility and birth defects. The risk of developmental failures in woman, such as chromosome abnormalities and early pregnancy loss increases about 5-10 years earlier than the menopause, which may be due to age-related decreases in oocyte quality [6]. In most developed countries, the typical age at first birth has delayed and the demand for assisted reproductive technology has increased [7]. The importance of evaluating oocyte quality has increased due to the general trend of promoting single embryo transfer to avoid multiple pregnancies and the development of technologies for oocyte cryopreservation. Although the age-related decreases in oocyte quality is a social and medical concern, the mechanisms have not yet been elucidated.

Ca^{2+} waves (increase in calcium ion concentration) propagate through the oocyte during fertilization, which activate the oocyte and induce embryonic development [8]. They trigger several processes such as resumption of meiosis, release of surface granules, and formation of the pronucleus, which are collectively called oocyte activation, and initiate embryonic development [9]. Ca^{2+} waves are found in almost all animal species and are caused by Ca^{2+} channels called inositol 1, 4, 5-trisphosphate (IP3) receptors on the endoplasmic reticulum, which functions as an intracellular Ca^{2+} store [9][10]. The pattern of Ca^{2+} response is associated with development of embryo. Although the spatiotemporal patterns of Ca^{2+} response vary from species to species, ranging from single transient (e.g. amphibians, nematode) to oscillations (e.g. mammals), Ca^{2+} responses are key process for oocyte activation [9][11]. The ability to generate Ca^{2+} waves is acquired in mammalian oocytes during meiotic maturation [12]. The excessive or too low Ca^{2+} transits influence post-implantation development of the embryo or the embryo implantation [13]. The peak of Ca^{2+} response in mature mouse oocytes has higher amplitude and lasts longer than in immature oocytes [14][15][16]. The meiotic maturation in oocyte cytoplasm, such as reorganization of endoplasmic reticulum, the main Ca^{2+} storage, and increase in the number of IP3 receptors, may cause the differences in the patterns of Ca^{2+} response [12]. The normal pattern Ca^{2+} response can be seen as an indicator of sufficient maturation of oocytes. The impact of maternal aging on mechanisms of generating Ca^{2+} responses in fertilized oocytes has not been thoroughly examined. The recent study has reported that maternal aging differently affects the amounts of Ca^{2+} stored in the oocytes and expression of genes involved in the regulation of the Ca^{2+} oscillations in those mouse types [17]. Although the fertilization Ca^{2+} waves are key process for embryonic development, mechanisms underlying generation of Ca^{2+} waves have not been fully elucidated.

The quantitative and mathematical analyses of phenomena in oocytes related to fertilization and developmental ability can be helpful to understand the mechanisms. The mechanisms of the phenomena in oocytes related to fertilization and developmental ability remain poorly understood. While there are many studies analyzed the phenomena based on biological experimental approaches, few studies quantitatively and mathematically analyzed them based on informatics approaches. The quantitative and mathematical analyses are expected to provide new biological findings that differ from those derived from biological experimental approaches.

The age-related changes in oocyte quality and the Ca^{2+} wave in *Caenorhabditis elegans* (*C. elegans*) can be analyzed by using imaging data of oocytes. The oocyte quality is thought to be reflected in oocyte appearance in *C. elegans* [18][19]. *C. elegans* cells can be noninvasively observed with high contrast by using Nomarski differential interference contrast (DIC) microscopy, which produce contrast by visually displaying the optical phase gradient [20][21]. The changes in oocyte appearance in *C. elegans* with aging can be captured by DIC microscopy, which would reflect the changes in oocyte quality with aging. The spatiotemporal dynamics of Ca^{2+} wave can be visualized using a fluorescent Ca^{2+} indicator. Takayama and Onami visualized the Ca^{2+} wave in *C. elegans* by high-speed confocal microscopy and image analysis [22]. Quantitative analyses of these phenomena, the age-associated changes in oocyte appearance and the spatiotemporal dynamics of fertilization Ca^{2+} wave, using in vivo imaging data may lead to new findings regarding phenomena in oocytes related to fertilization and developmental ability.

1.2 Objectives of the Study

This dissertation focuses on the age-related changes in oocyte quality and the fertilization Ca^{2+} wave as important phenomena for fertilization and development ability of oocytes. The purpose of this study is to provide new findings and insights regarding the phenomena related to the fertilization and developmental ability of oocytes. To this purpose, I perform quantitative and mathematical analyses of in vivo imaging data of oocytes in *C. elegans* as a model organism.

Firstly, I focus on the oocyte appearance that are thought to reflect oocyte quality. To examine whether the age-associated changes in appearance of *C. elegans* oocytes can be quantitatively characterized, I apply statistical image processing to the DIC images in oocytes (Chapter 3).

Secondly, to examine whether the genes involved in reproductive aging can be predicted, I screen for genes whose knockdown significantly changes the image features that characterize the age-associated changes in appearance (Chapter 4).

Finally, I focus on Ca^{2+} wave during fertilization. To propose a model of the Ca^{2+} wave that can represent more similar wave form to the observed one compared to the previous model, I modify the previous Ca^{2+} wave model (Chapter 5).

1.3 Outline of Dissertation

The dissertation is organized into the following chapters:

Chapter 1: The current chapter provides a research background and objectives of the research.

Chapter 2: This chapter presents an introduction of nematode *C. elegans.* It also introduces the related studies.

Chapter 3: This chapter describes the quantification of age-associated changes in cytoplasmic texture in *C. elegans* oocytes by using statistical image processing.

Chapter 4: This chapter describes the prediction of genes involved in reproductive aging by applying the image features proposed in chapter 3 to the image data obtained from large-scale gene silencing experiments.

Chapter 5: This chapter describes the improvement and evaluation of mathematical model for the fertilization Ca^{2+} wave in *C. elegans*.

Chapter 6: The final chapter gives conclusive discussion of the findings and suggestions for future work.

Chapter 2

Preparing for the Study

2.1 Model Organism *Caenorhabditis elegans*

Caenorhabditis elegans (*C. elegans*) has been developed as a model organism since Sydney Brenner began using it to study the genetics of development and neurobiology [23]. Since then, the cell lineage and the neuronal wiring have been determined [21][24]. *C. elegans* became the first multicellular organism to have its genomic DNA completely sequenced [25]. RNA interference, which is a mechanism to specifically silence genes triggered by double-stranded RNA, was first discovered in *C. elegans* in 1998 [26]. Today, *C. elegans* is a powerful model organism for the study of universal mechanisms of life in many fields including genomics, cell biology, neuroscience and aging.

C. elegans is a free-living transparent nematode about 1 mm in length that lives in the soil environments. *C. elegans* has two sexes, males and self-fertilizing hermaphrodites. Hermaphrodites lay mostly hermaphroditic progeny and produce males at a very low frequency (about 0.1%) by non-disjunction [27]. Hermaphrodites are composed of 959 somatic cells and have basic anatomy including pharynx, intestine, gonad, nerve, and muscle. *C. elegans* cells can be observed by using Nomarski differential interference contrast microscope because of the transparency of *C. elegans*' body [20][21].

The gonads are composed of U-shaped tubes joined to central uterus. In hermaphrodites, approximately 300 sperm are produced before switching to oogenesis after the adult molt. Germ cells leave the proliferative zone, undergo meiotic development and progress gametogenesis in an assembly-line fashion. Germ cells proceed through the pachytene stage of meiotic prophase in the distal arm and progress to diakinesis, where they arrest until meiotic maturation in the proximal arm. Mature oocytes are transported to the spermatheca for fertilization, and the resulting embryos are pushed into the uterus and then laid through the vulva.

The *C. elegans* is a leading model for studying aging because of its short lifespan (~ 3 weeks) and the conservation of longevity pathways from *C. elegans* to humans [28]. *C. elegans* also undergoes reproductive senescence and ceases reproducing progeny after one third of their lifespan [29]. Like the increase in chromosome nondisjunction as human females age, aging *C. elegans* exhibits increased chromosome nondisjunction during aging, suggesting conserved consequences of germline aging [30].

2.2 Age-related Decreases in Oocyte Quality

Advanced maternal age causes decrease in oocyte quality and poor assisted reproductive technology (ART) outcomes [31]. Oocytes from advanced maternal age exhibit increased errors in fertilization, chromosome segregation, and embryonic cleavage [6][32][33]. Embryonic aneuploidy is a most frequent cause of developmental errors in mammals [6][34]. It has been well established that increasing maternal age leads to a higher risk of chromosomal aneuploidy, which is largely explained by the meiotic non-disjunction [35][36]. Several processes have been suggested as direct or indirect causative for chromosome segregation errors : dysfunctional cohesins, reduced stringency of spindle-assembly checkpoint, shortening of telomeres, and impaired mitochondrial metabolic activity [31].

Oocyte morphology is a parameter to evaluate oocyte quality for in vitro fertilization and intracytoplasmic sperm injection (ICSI) [37][38]. The morphological features related to the cumulus cells, polar body, and cytoplasm appear to be associated with oocyte quality [39]. However, morphological evaluations for grading oocyte quality are still controversial due to lack of objectivity and biological evidence. Although most studies examined relationship between morphological features and developmental success rates, the morphological features are not clearly associated with biological intrinsic factors. One reason is that no methods are established to objectively evaluate the morphological features related to oocyte quality with consistency.

To overcome subjectivity of morphological observations in ART, the automatic systems and prediction models based image processing or machine learning have been proposed [40][41]. Although they enable to evaluate the morphological features more objectively, they do not clearly link the morphological features to biological intrinsic factors.

2.3 Fertilization Ca^{2+} Waves

Ca^{2+} waves are essential for activation of the embryo development. They trigger several processes such as resumption of meiosis, establishment of the block to polyspermy, and formation of the pronucleus [9]. The increase in calcium ion concentration is mainly due to Ca^{2+} release from the endoplasmic reticulum and forms a wave that starts from the point of sperm entry and propagates the Ca^{2+} signal through the whole egg.

The artificial stimulus instead of the natural stimulus provided by sperm can also trigger oocyte activation and initiate development [42]. Artificial oocyte activation by applying chemical agents, such as the Ca^{2+} ionophore can be used to overcome fertilization failure after ICSI.

The mechanisms that the sperm induces Ca^{2+} rise in oocyte have not been fully understood. Three major hypotheses were proposed to understand the mechanisms: (1) the sperm factor model [43][44], (2) the ligand-receptor interaction model [45], and (3) the sperm Ca^{2+} model [46][47]. The sperm factor model assumes that sperm soluble factor induces Ca^{2+} release after sperm-oocyte fusion [9][48]. The ligand-receptor model assumes that egg activation is triggered by an interaction between a ligand upon the sperm and a receptor on the egg [49][50][51]. The sperm Ca^{2+} model assumes that the initial Ca^{2+} rise induced by a bolus of Ca^{2+} stored in sperm (bomb model [46]) or by Ca^{2+} entry via channels in the surface membrane of sperm (conduit model [47]). The initial Ca^{2+} rise induces a release of Ca^{2+} from the endoplasmic reticulum via Ca^{2+}-induced Ca^{2+}-release mechanism. Although these three mechanisms have been proposed and evaluated, the supported mechanisms vary from species to species and the underlying mechanisms have been unclear.

To understand the mechanisms underlying generating of Ca^{2+} waves, the mathematical models of *Xenopus* Ca^{2+} wave have been suggested [52][53]. Takayama and Onami previously quantified and proposed a reaction-diffusion model of Ca^{2+} wave in *C. elegans* [22]. Mathematical models of Ca^{2+} waves would help to understand the mechanisms of generating Ca^{2+} waves.

Chapter 3

Quantification of the Changes in Cytoplasmic Texture Associated with Aging by Statistical Image Processing

3.1 Introduction

Oocyte quality is an important factor in the success of animal development. Oocyte quality decreases with aging, thereby increasing errors in fertilization, chromosome segregation, and embryonic cleavage [6][32][33]. However, the mechanisms underlying the age-related decrease in oocyte quality remain incompletely understood.

The nematode *Caenorhabditis elegans* (*C. elegans*) is a leading model for studying aging because of its short lifespan (~ 3 weeks) and the conservation of longevity pathways from *C. elegans* to humans [28]. In particular, *C. elegans* has been developed as a model for studying age-related decline in fertility [18]. Mutant analyses using *C. elegans* have revealed various genes and signaling pathways that affect aging [54][55][56]. The molecular processes involved in the age-related regulation of oocyte quality are shared between *C. elegans* and mammals [19].

In *C. elegans* hermaphrodites, sperms are produced during the larval stage and stored in the spermatheca; oocytes are produced continually during the adult stage. Mature oocytes are transported to the spermatheca for fertilization, and the resulting embryos are pushed into the uterus and then laid through the vulva (Figure 3.1a). The number of progeny produced on each day decreases with aging and self-reproduction ceases after about 5 days of adult life [57][58]. In young animals, almost all transported oocytes are fertilized and almost all fertilized eggs are viable; in contrast, older animals produce a substantial number of unfertilized oocytes and inviable eggs, suggesting that oocyte quality declines with aging [19].

Age-related changes in oocytes are found not only in function but also in appearance [18][19][33]. In *C. elegans*, aged oocytes shrink, the contacts between oocytes become loose, and oocytes fuse into large clusters [18][19]. Although there is no method that can objectively quantify age-related changes in oocyte appearance, information provided by such a method could be used to clarify the relationship between changes in the quality of oocytes and their appearance with aging.

Image processing of cell appearance has been applied to various branches of biomedical research, including the identification of malignant cells and detection of cancer [59][60], analysis of morphological changes [61], and the classification of cell populations with different functions [62][63]. Texture analysis is one method of classifying biomedical images [64]. In addition, modern machine learning methods, such as deep learning, have recently been applied to various biological applications [65]. The analysis of cell appearance by using image processing is an effective way to characterize and classify the status of cells.

The Gray Level Co-occurrence Matrix (GLCM) is a well-known statistical method for examining textures and is widely used to describe spatial properties [66]. The GLCM approach has been used in various biomedical applications, including cell recognition, evaluation of ultrastructural changes, and textural classification of medical images [61][67][68][69]. For an image with G gray levels, the GLCM is an estimate of the second-order joint probability $P(i, j \mid d, \theta)$ of two pixels with gray levels i and j ($0 \leq i < G$, $0 \leq j < G$) that are d pixels apart from each other along direction θ.

To objectively describe changes in the appearance in oocytes with aging, I used Nomarski differential interference contrast (DIC) microscopy to view and characterize *C. elegans* oocytes. Nomarski DIC microscopes produce contrast by visually displaying the optical phase gradient. DIC microscopy can capture images of transparent objects without chemical staining and is widely used to observe nuclei, nucleoli, and granular structures within *C. elegans* cells [20][21]. I focused on the cytoplasmic texture because I consider that it reflects the internal status of oocytes more directly than does morphologic appearance, such as the size or shape of oocytes. To quantify the age-associated changes in the cytoplasmic texture of *C. elegans* oocytes, I propose the image feature “Max-min Value” (Mm Value) for measuring textural roughness. I used Mm Value and the GLCM approach to reveal quantitative differences between young and aged oocytes.

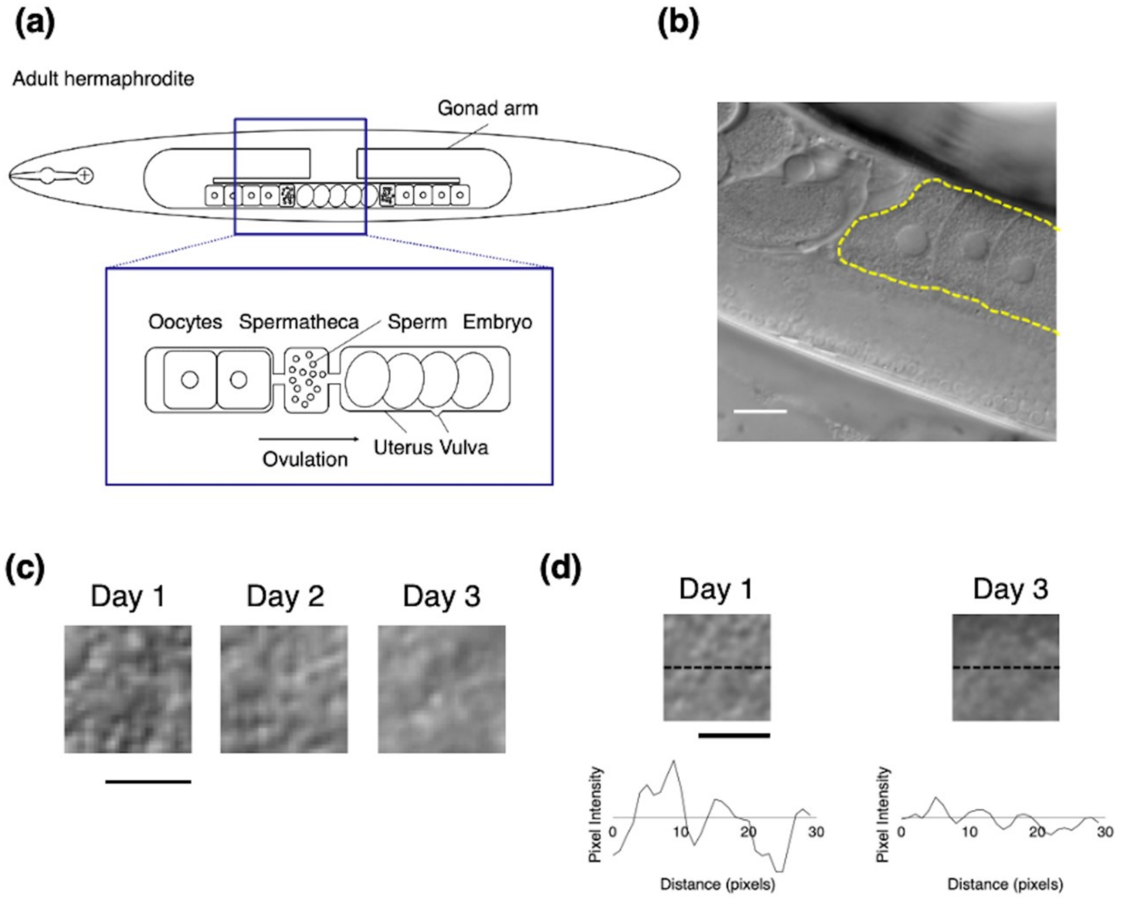

Figure 3.1 Observation of *Caenorhabditis elegans* oocytes by using Nomarski differential interference contrast microscopy.

(a) Schematic representation of an adult hermaphroditic gonad. Oocytes mature and enter the spermatheca, where they are fertilized by the accumulated sperm. Embryos are pushed into the uterus and then laid through the vulva. (b) Representative differential interference contrast image of oocytes in a gonad. The dotted yellow line surrounds the oocytes. Scale bar, 20 µm. (c) Examples of extracted images of the cytoplasmic texture in oocytes from Day 1, Day 2, and Day 3 adults. Scale bar, 5 µm. (d) Cytoplasmic texture images and profile plots of Day 1 and Day 3 oocytes. The dotted black line indicates the position of the horizontal profile plot. Scale bar, 5 µm.

3.2 Results

3.2.1 Mm Value Reflects Age-associated Changes in the Cytoplasmic Texture of *C. elegans* Oocytes

To quantify age-associated changes in oocyte appearance, I used Nomarski DIC microscopy to observe the oocytes of 1-, 2-, and 3-day-old *C. elegans* adults (hereafter called Day 1, Day 2, and Day 3 adults, respectively). I observed that the fertilized embryos developed successfully in the Day 1 and Day 2 adults, whereas those in the Day 3 adults exhibited developmental failure, such as errors in egg shell formation or embryonic cleavage, suggesting that fertility declines in the first 3 days of the reproductive span. I therefore focused on quantifying age-associated changes in oocyte appearance in the DIC images over this 3-day period. In DIC microscopic images, the nucleus appears as a smooth, round region in the center of the oocyte, and the cytoplasm is rough (Figure 3.1b). As previously reported [18] [19], I noted various morphologic differences (accumulation of oocytes, oocyte size, cavities, and cluster formation) between Day 1 and Day 3 adults. In addition, visual comparison of the images showed that the oocyte cytoplasmic texture was rougher in appearance in Day 1 than Day 3 worms (Figure 3.1c). In a simple comparison of pixel intensities along a line across the oocytes, Day 1 worms showed larger changes in pixel intensity than Day 3 worms (Figure 3.1d).

To examine whether the texture changes can be characterized quantitatively, I performed a computational texture analysis of the oocyte cytoplasm. To this end, I defined an image feature, the "Max-min Value (Mm Value)," as follows. Mm Value is calculated by a moving window operation. The maximum and minimum intensities within a moving window of W×W pixels are obtained. Then the difference between maximum and minimum intensities is calculated. Mm Value is defined as the mean of the differences calculated by applying the moving window to the entire image (Figure 3.2a). In a rough-texture image, the Mm Value is expected to be high, whereas in a smooth-texture image, the Mm Value is expected to be low.

I observed that the Day 3 Mm Value was significantly smaller than that for Days 1 and 2 when a moving window of 3×3 pixels was used (n = 12 animals in each age group; Figure 3.2b; and Figure 3.3). Mm Value did not differ significantly between Days 1 and 2. These results suggest that the Mm Value decreases with aging and can be used to quantitatively characterize the age-associated changes in the cytoplasmic texture of *C. elegans* oocytes.

To examine whether general first-order statistics quantitatively characterize the age-associated changes in cytoplasmic texture, I calculated "SD" and "entropy", which are the mean standard deviation and entropy of local pixel intensities in a moving window. I set the size of the moving window to 3×3 pixels. Similar to the Mm Value, the SD was significantly smaller on Day 3 than Days 1 and 2 and did not differ significantly between Days 1 and 2 (n = 12 animals in each age group; Figure 3.2c). In contrast, entropy was similar among all 3 age groups (n = 12 animals in each age group; Figure 3.2d). Therefore, the change in cytoplasmic texture in aging *C. elegans* oocytes could be characterized quantitatively by using the Mm Value or SD.

To compare the performance of Mm Value, SD, and entropy, I used various sizes of moving window ranging from 3×3 to 29×29 pixels (Figure 3.2e–g). The Mm Value and SD were significantly smaller on Day 3 than Day 1 for smaller window sizes (3×3 to 17×17 pixels for Mm value and 3×3 to 7×7 pixels for SD; Figure 3.2e and f); the difference between Day 3 and Day 1 was significant for a broader range of window sizes in the case of Mm value. Entropy showed no significant difference between the three age groups at any window size (Figure 3.2g).

To examine whether the properties of the first-order statistics are consistent in other datasets, I calculated the Mm Value, SD, and entropy in another dataset (n = 10 animals each at Day 1 and Day 3). As with the first dataset, the Mm Value and SD were significantly smaller on Day 3 than Day 1 for smaller window sizes (3×3 to 25×25 pixels for Mm value and 3×3 to 11×11 pixels for SD; Figure 3.4a and b), and the difference between Day 3 and Day 1 was significant for a broader range of window sizes in the case of Mm value. However, unlike with the first dataset, the entropy was significantly smaller on Day 3 than Day 1 when using smaller window sizes (3×3 to 11×11 pixels; Figure 3.4c).

My finding that, in both datasets, the Mm Value was significantly smaller on Day 3 than Day 1 for a broader range of window sizes than that observed for SD and entropy (Figure 3.2e–g; Figure 3.4) suggests that, compared the other two first-order statistics, Mm Value more robustly characterizes the age-associated changes in cytoplasmic texture.

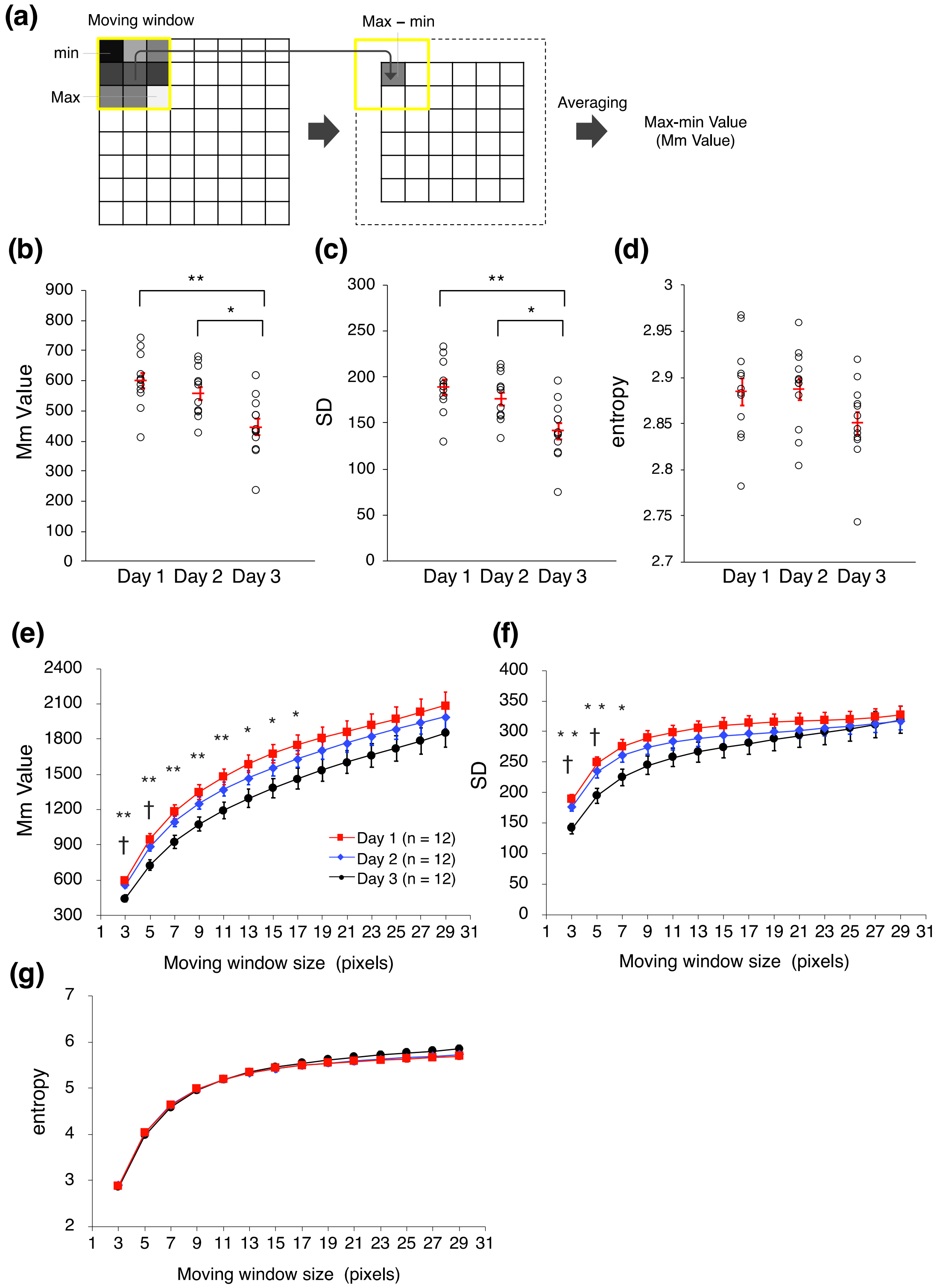

Figure 3.2 First-order statistical analysis of the age-associated changes in the cytoplasmic texture of *Caenorhabditis elegans* oocytes.

(a) Algorithm for calculating the Max-min Value (Mm Value), which is the mean of the difference between the maximum and minimum intensities within each moving window. (b–d) Comparison of the first-order statistical features of (b) Mm Value, (c) SD, and (d) entropy (3×3-pixel window) between Day 1, Day 2, and Day 3 oocytes. Circles indicate individual animals (n = 12 animals in each age group, pooled from two experiments); red bars indicate the mean values. Error bars indicate SEM. Asterisks indicate statistical significance (*$P < 0.05$, **$P < 0.01$; Tukey–Kramer test). (e–g) Comparison of (e) Mm Value, (f) SD, and (g) entropy between Day 1, Day 2, and Day 3 oocytes by using window sizes of 3×3 to 29×29 (n = 12 animals in each age group, pooled from two experiments). Symbols indicate statistical significance (Tukey–Kramer test) between Day 1 and Day 3 oocytes (*$P < 0.05$, **$P < 0.01$) or Day 2 and Day 3 oocytes (†$P < 0.05$). Error bars indicate SEM.

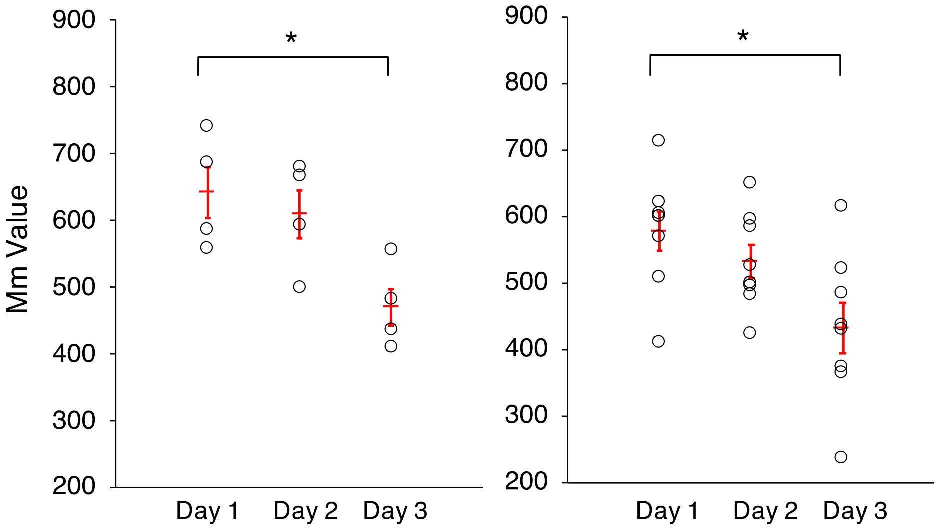

Figure 3.3 Comparison of the Max-min Value between Day 1, Day 2, and Day 3 oocytes in each of two experiments.

Max-min Value (Mm Value) was calculated by using a 3×3-pixel window in Day 1, Day 2, and Day 3 oocytes. Circles indicate individual animals (n = 4 or 8 animals each age group); red bars indicate the mean values. Error bars indicate SEM. Asterisks indicate statistical significance (*$P < 0.05$; Tukey–Kramer test).

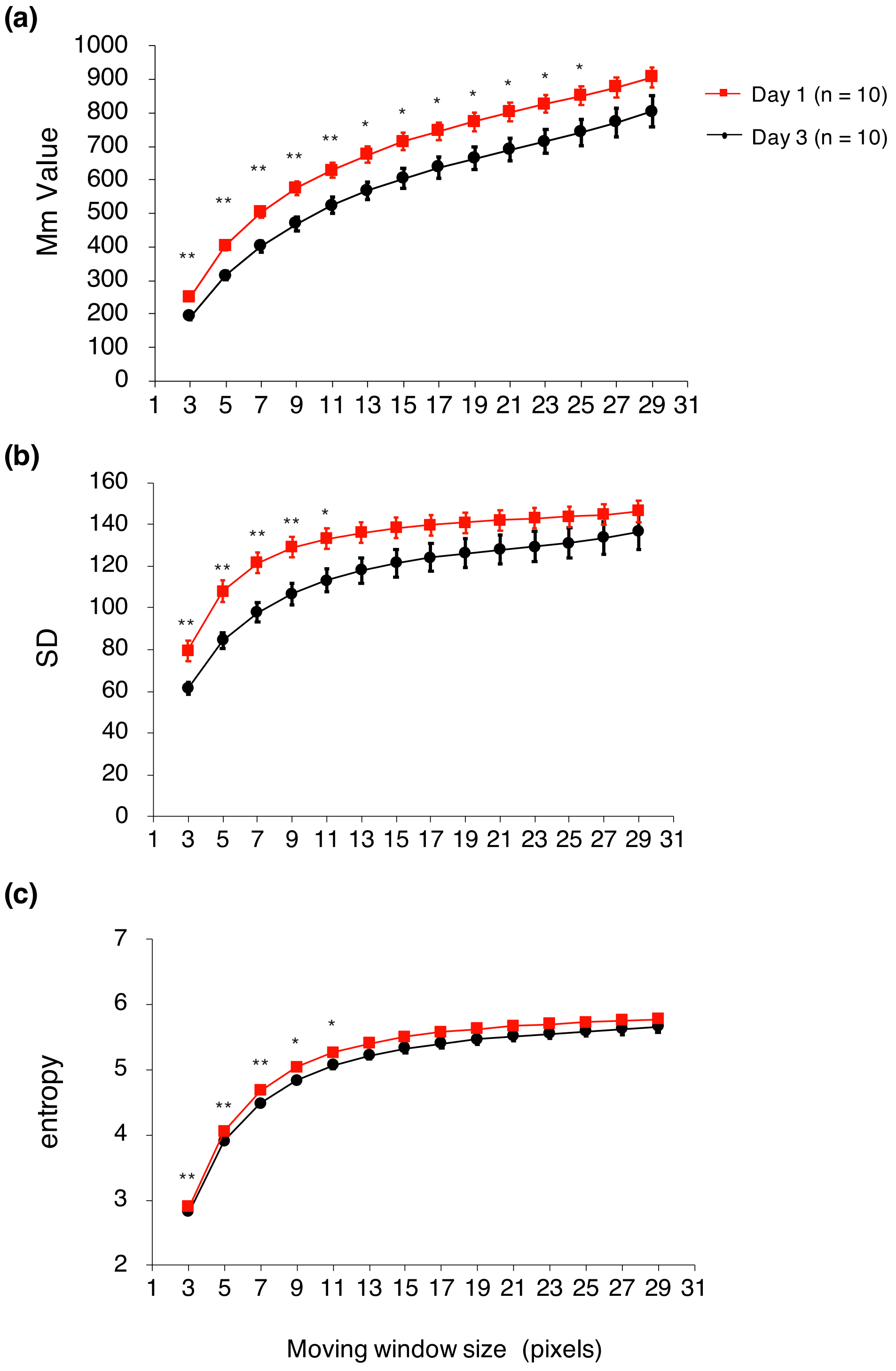

Figure 3.4 Comparison of Max-min Value, SD, and entropy between Day 1 and Day 3 oocytes.

Various window sizes from 3×3 to 29×29 pixels were used. Data are means ± SEM (n = 10 animals in each age group). Asterisks indicate statistical significance between Day 1 and Day 3 oocytes (*$P < 0.05$, **$P < 0.01$; Welch's two-tailed *t* test).

3.2.2 The second-order statistic GLCM varies with the age-associated changes in cytoplasmic texture in *C. elegans* oocytes

GLCM is an estimate of the second-order joint probability $P(i, j \mid d, \theta)$ that two pixels with gray levels i and j are d pixels apart from each other in the direction θ (Figure 3.5a) [66]. To examine whether a second-order statistic more significantly characterizes age-associated texture changes than Mm Value, I used the GLCM-based texture feature *Correlation* (COR), which is a measurement of the gray-level linear dependencies of pixels at specified positions relative to each other. I calculated the COR of the cytoplasmic texture of Day 1, Day 2, and Day 3 oocytes.

As the d value increased, COR decreased and converged to around zero (Figure 3.5b–e). For various θ values, the d value at which COR converged to zero was larger in Day 3 oocytes than in Day 1 or 2 oocytes; for example, for θ = 135, COR in Day 3 oocytes converged to zero when $d = 5$, whereas COR in Day 1 or Day 2 oocytes converged to zero when $d = 2$ (Figure 3.5e). I found that, at several levels of the parameters d and θ, COR was significantly larger in Day 3 oocytes than in Day 1 and Day 2 oocytes. In particular, the smallest P value was obtained for the comparison of COR in Day 3 oocytes versus Day 1 oocytes when $d = 1$ and $\theta = 135$ ($P = 1.0\times10^{-8}$; n = 12 animals in each age group; Tukey–Kramer test). The P value for this parameter set was four orders of magnitude lower than the lowest P value obtained by using Mm Value (window size, 3×3 pixels; $P = 6.0\times10^{-4}$; n = 12 animals in each age group; Tukey–Kramer test). These results suggest that COR effectively characterized the age-associated changes in cytoplasmic texture. COR was able to more significantly characterize the differences between Day 1 and Day 3 oocytes than the Mm Value did when using an appropriate parameter set. In addition to COR, I tested several texture-associated features based on GLCM, including *Angular Second Moment* (ASM), *Contrast* (CON), *Inverse Difference Moment* (IDM), and *Entropy* (ENT), but COR continued to yield the best characterization (Figure 3.6).

In general, for all oocytes regardless of age, COR obtained when θ = 135 was smaller than that obtained with the other angles tested at equivalent d (Figure 3.5f–h).

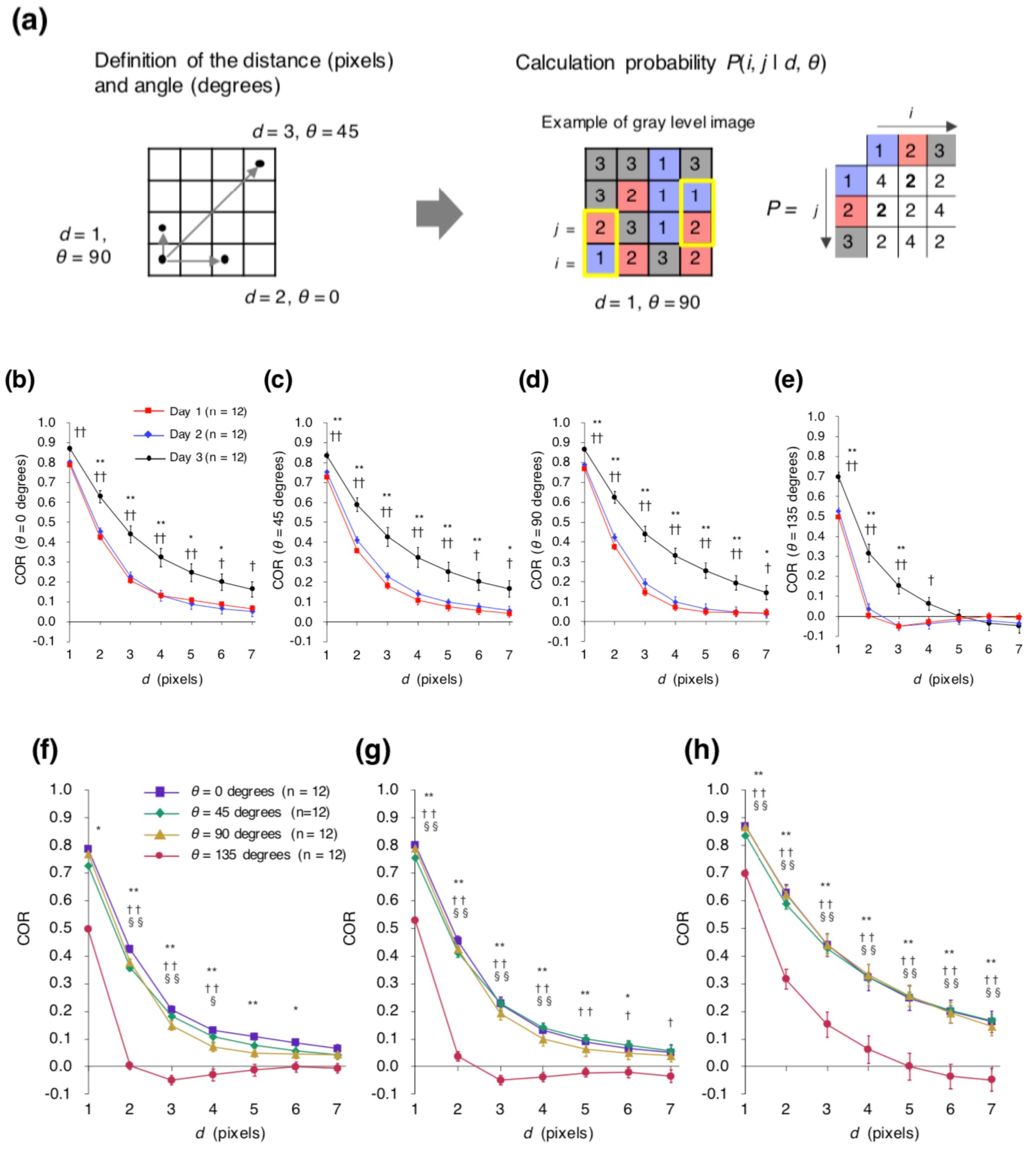

Figure 3.5 Second-order statistical analysis of the age-associated changes in the cytoplasmic texture of *Caenorhabditis elegans* oocytes.

(a) Algorithm for calculating the Gray Level Co-occurrence Matrix (GLCM). First, I define a spatial relationship by using the parameters distance (d) and angle (θ). I then calculate the second-order joint probability $P(i, j \mid d, \theta)$ of two pixels with gray levels i and j ($0 \leq i < G$, $0 \leq j < G$). To calculate $P(i, j \mid d, \theta)$, I sum the number of pixels with paired intensities (i and j) in the defined spatial relationship. For example, when d is 1 pixel and the θ is 90 degrees, the calculated number of pixels with $i = 1$ and $j = 2$ or $i = 2$ and $j = 1$ is 2. The co-occurrence matrix defined is symmetric. (b–e) Effect of oocyte age on *Correlation* (COR). Curves of mean COR as a function of distance d for Day 1, Day 2, and Day 3 oocytes are shown for θ set at (b) 0, (c) 45, (d) 90, and (e) 135 degrees. Data are means ± SEM (n = 12 animals in each age group, pooled from two experiments). Symbols indicate significant difference (Tukey–Kramer test) in COR between Day 1 and Day 3 oocytes (*$P < 0.05$, **$P < 0.01$) or Day 2 and Day 3 oocytes (†$P < 0.05$, ††$P < 0.01$). (f–h) Effect of θ on COR. Curves of mean COR as a function of distance d when θ is set at 0, 45, 90, or 135 degrees are shown for (f) Day 1, (g) Day 2, and (h) Day 3 oocytes. Data are means ± SEM (n = 12 animals in each age group, pooled from two experiments). Symbols indicate significant difference (Tukey–Kramer test) in COR between 0 and 135 degrees (*$P < 0.05$, **$P < 0.01$), 45 and 135 degrees (†$P < 0.05$, ††$P < 0.01$), or 90 and 135 degrees (§$P < 0.05$, §§$P < 0.01$).

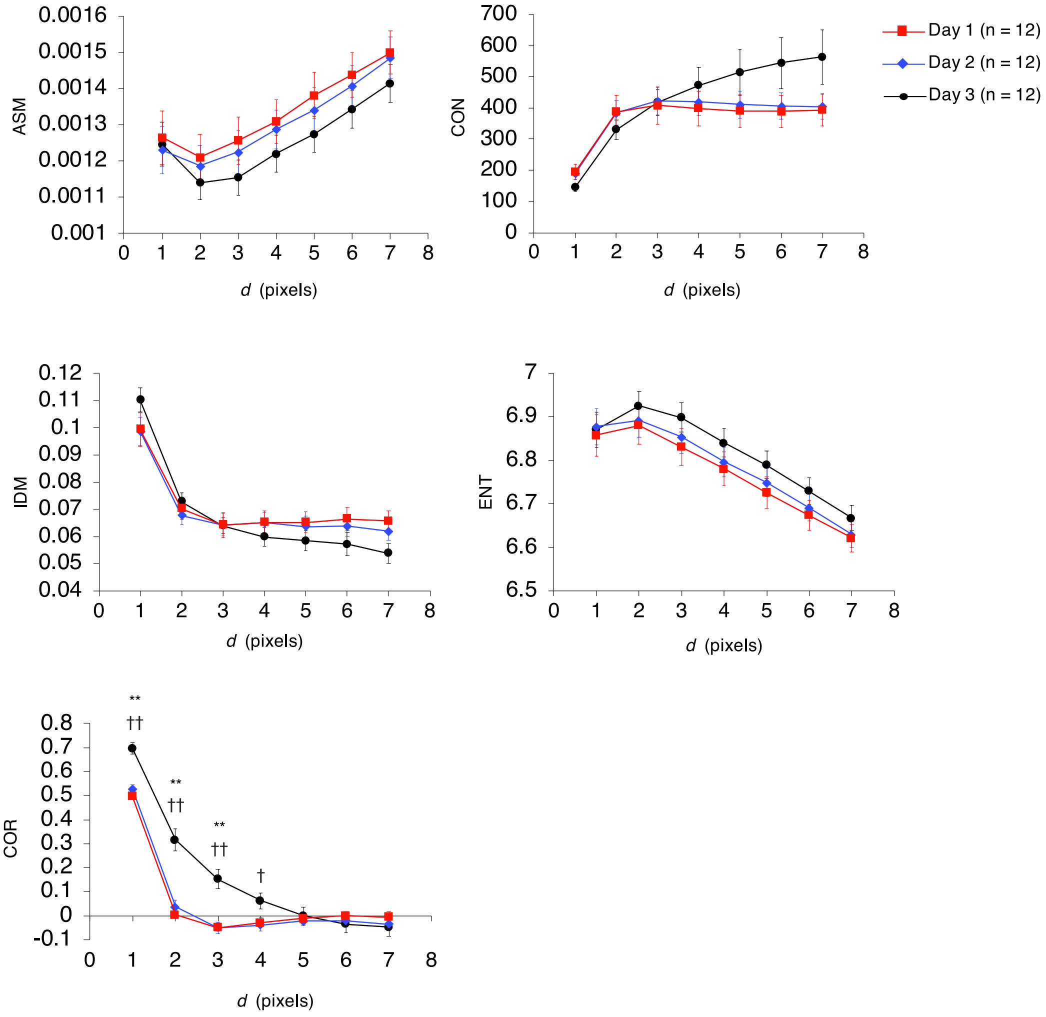

Figure 3.6 Comparison of key texture features based on a Gray Level Co-occurrence Matrix between Day 1, Day 2, and Day 3 oocytes.

Curves of the indicated texture features as a function of distance d when $\theta = 135$ are shown. Data are means ± SEM (n = 12 animals each age group, pooled from two experiments). ASM, *Angular Second Moment*; CON, *Contrast*; IDM, *Inverse Difference Moment*; ENT, *Entropy*; COR, *Correlation*. Symbols indicate statistical significance (Tukey–

Kramer test) between Day 1 and Day 3 oocytes (*$P < 0.05$, **$P < 0.01$) or Day 2 and Day 3 oocytes (†$P < 0.05$, ††$P < 0.01$). Second-order statistical analysis of the age-associated changes in the cytoplasmic texture of *Caenorhabditis elegans* oocytes.

3.2.3 Sample Orientation does not Influence the Dependency of COR on the Angle θ

Images from DIC microscopy have a shadow-cast appearance oriented in the shear direction of the prism [70]. The texture characterized by using COR was dependent on θ, i.e., COR was smaller at $\theta = 135$ than at any other angle (Figure 3.5f–h). To examine whether this angle dependency is due to either the orientation of the worm or the imaging system itself, I calculated COR after rotating worm samples to 0, 45, 90, or 135 degrees relative to horizontal (i.e., 0 degrees) (Figure 3.7a–d). If sample orientation causes the angle dependency, then the angle-dependent property of COR should change depending on sample orientation. Conversely, if the angle dependency is due to the imaging system itself, then orientation should have no effect on this property. I found that, regardless of sample orientation, COR was smaller at $\theta = 135$ than at other angles (n = 10 animals in each angle group; Figure 3.7e–h). This result indicates that the angle-dependent property of COR measurements of oocyte cytoplasmic texture is due to the imaging system itself, rather than to the orientation of the worm imaged.

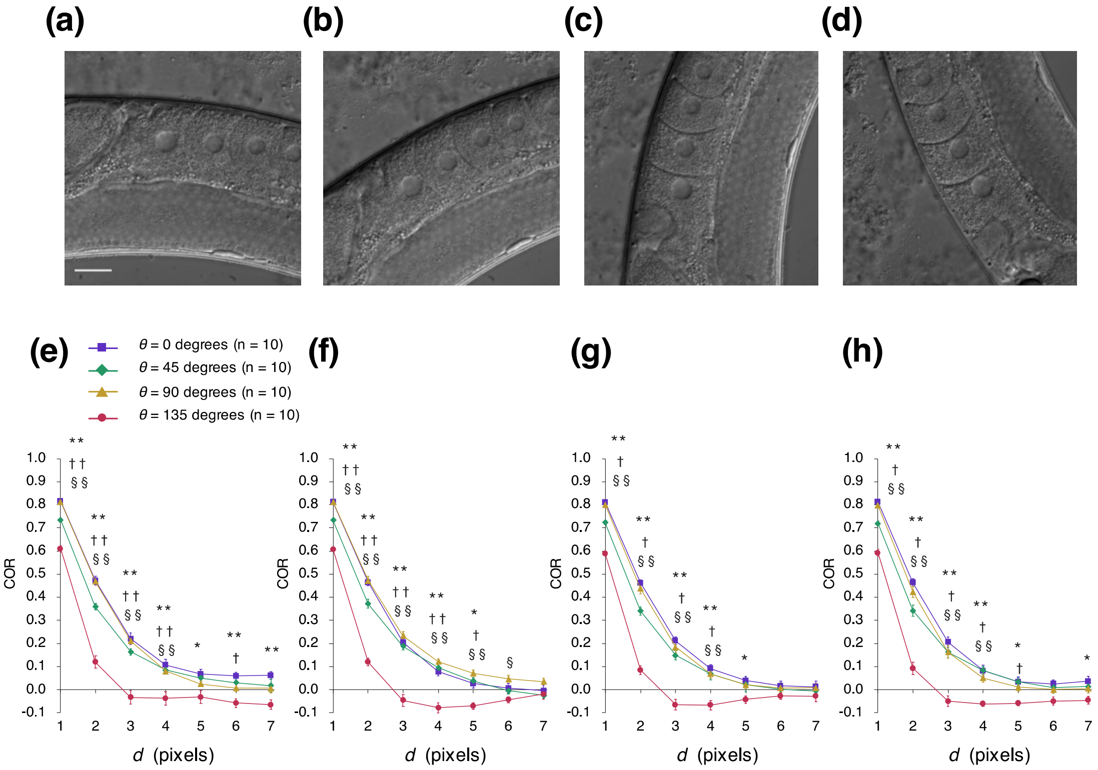

Figure 3.7 Comparison of *Correlation* between angle parameters by using rotated worms.

(a–d) Representative images of worms rotated (a) 0, (b) 45, (c) 90, or (d) 135 degrees from horizontal (0 degrees). Scale bar, 20 μm. (e–h) Effect of worm rotation on *Correlation* (COR). Curves of mean COR as a function of distance *d* are shown for worms rotated (e) 0, (f) 45, (g) 90, and (h) 135 degrees from horizontal. Data are means ± SEM (n = 10 animals in each angle group). Symbols indicate significant difference (Tukey–Kramer test) in COR between 0 and 135 degrees ($^{*}P < 0.05$, $^{**}P < 0.01$), 45 and 135 degrees ($^{\dagger}P < 0.05$, $^{\dagger\dagger}P < 0.01$), or 90 and 135 degrees ($^{\S}P < 0.05$, $^{\S\S}P < 0.01$).

3.2.4 The Optimal Choice of Distance Parameter *d* Depends on the Resolution of the Image

To examine whether the optimal choice of the GLCM parameter *d* to characterize the age-associated changes depends on the resolution of the image, I calculated the COR in upscaled and downscaled images created by artificially changing the resolution of the original images (Figure 3.8a–c). The COR in Day 1 and 3 oocytes converged to zero at smaller *d* in the downscaled images than in the original images (Figure 3.8d and e). In contrast, COR converged at larger *d* in the upscaled images than in the original images (Figure 3.8e and f). In both the original and rescaled images, the *d* value at which COR converged was larger in Day 3 oocytes than in Day 1 oocytes (Figure 3.8d–f). The smallest *P* value was obtained for the comparison of COR in Day 3 oocytes versus Day 1 oocytes in the downscaled, original, and upscaled images when $d = 1$, 3, and 5, respectively ($P = 8.5\times10^{-5}$, 5.7×10^{-5}, and 5.5×10^{-5}; n = 10 animals in each age group; Welch's two-tailed t test; Figure 3.8d–f). These results suggest that the *d* value at which COR converges to zero and the optimal *d* value to characterize the age-associated changes in cytoplasmic texture increase as the image resolution increases, but the marked difference in the convergence properties of COR between Day 1 and Day3 oocytes is not changed by image resolution.

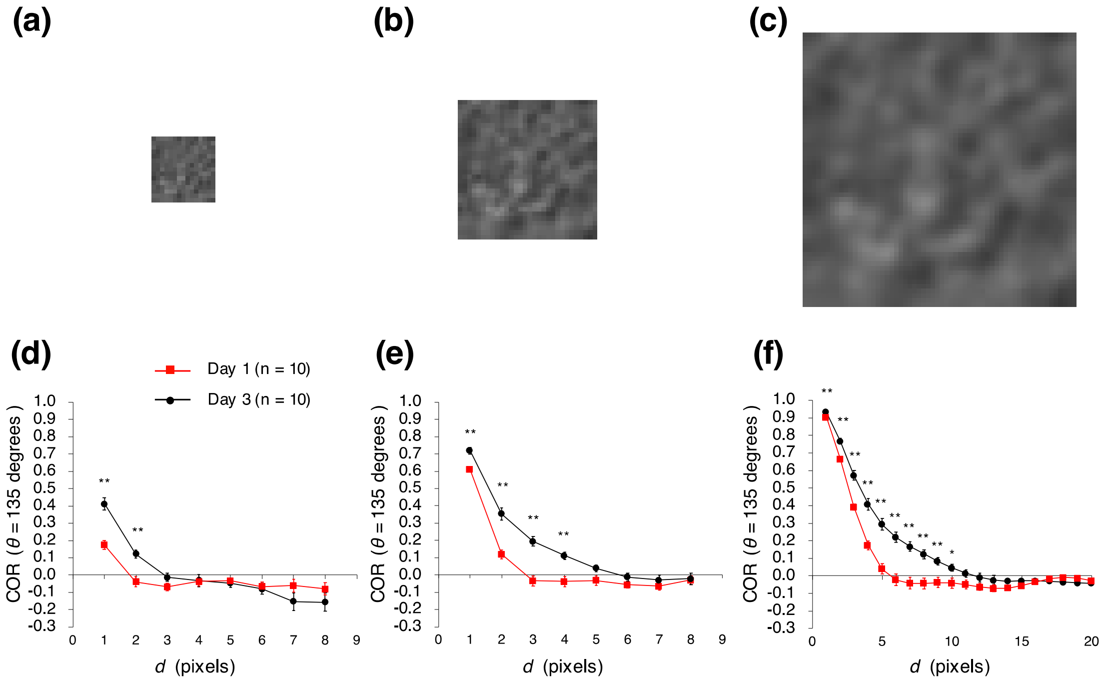

Figure 3.8 Comparison of *Correlation* between pseudo-low and pseudo-high resolution images.

(a–c) Representative original and rescaled images. The (b) original images (30×30 pixels) were (a) downscaled (final size, 15×15 pixels) to produce pseudo-low resolution images, and (c) upscaled (final size, 60×60 pixels) to produce pseudo-high resolution images. (d–f) Curves of mean *Correlation* (COR) as a function of distance *d* when $\theta = 135$ are shown for the (e) original, (d) pseudo-low resolution, and (f) pseudo-high resolution images. Data are means ± SEM (n = 10 animals in each age group; orientation of the worms is 0 degrees).

3.2.5 Changing Smoothness or Simulating Large Structures did not Reproduce the Age-associated Changes in Cytoplasmic Texture

To elucidate the factor that causes the age-associated texture change that is characterized by Mm Value or COR, I visually compared Day 1 and Day 3 oocytes. I considered two factors that might underlie the age-associated texture change characterized by Mm Value and COR: (1) cytoplasmic smoothness in oocytes (i.e., the cytoplasm of Day 3 oocytes appeared smoother than that of Day 1 oocytes) and (2) the distribution of large structures (i.e., large structures were distributed irregularly in the cytoplasm of Day 3 oocytes but the structure was homogenous throughout that of Day 1 oocytes) (Figure 3.9a).

To examine whether these factors caused the texture changes, I created 'Day 3-fied images' by applying image processing to Day 1 images. I created three patterns of Day 3-fied images by manipulating the factors. The first pattern, 'Smoothed Pattern,' was created by smoothing the images of Day 1 oocytes. That is, the maximum and minimum intensities of Smoothed pattern images were normalized to minimum + offset and maximum – offset, respectively by using the minimum and maximum intensities from Day 1 oocytes. The second pattern, ‘Large Structure Pattern’, was generated by applying a Gaussian filter multiple times to the center part of the Day 1 images; the parameter *iteration* dictates the number of times the filter is applied. I created the third pattern, ‘Combination Pattern’, by first smoothing the Day 1 images and then generating large structures on them (Figure 3.9b).

I then compared Mm Value and COR between Day 3-fied, actual Day 1, and actual Day 3 oocyte images (n = 10 animals in each age group; Figure 3.9c). I set the parameter *offset* in the Smoothed pattern to 50, 100, or 200 and the parameter *iteration* in the Large Structure pattern to 1, 3, or 5. If the properties of the Day 3-fied images are similar to the actual images, the features of the Day 3-fied images would be expected to be similar to those of actual Day 3 images and differ from those of actual Day 1 images. For Smoothed pattern images, Mm Value at a window size of 3×3 pixels for the Day 3-fied images did not differ significantly from actual Day 3 images but was significantly smaller than that of actual Day 1 images (Figure 3.9c; *offset* = 100, 200). When the Day 3-fied images were compared with Day 1 images, all of the three patterns of Day 3-fied images reproduced the difference in Mm Value between Day 1 and Day 3 oocytes (Figure 3.9c). In addition, for all patterns, the Day 3-fied images reproduced the differences in general first-order statistical features, SD and entropy, between Day 1 and Day 3 oocytes (Figure 3.10). Therefore, in terms of these features, all three patterns of Day 3-fied images were similar to actual Day 3 images.

Next, I calculated COR for the three patterns of Day 3-fied images and the actual Day 1 and Day 3 images (n = 10 animals in each age group). As mentioned above, for the actual images, COR converged to zero at larger d values for Day 3 than for Day 1 (Figure 3.5b–e). However, COR of Day 3-fied images converged to zero at almost the same d as the Day 1 images for the Smoothed and Large Structure patterns (Figure 3.9d and e), and the Combination Pattern (Figure 3.11). Therefore, none of the three patterns of Day 3-fied images accurately represented the differences in COR between actual Day 1 and Day 3 images. This finding suggests that the age-associated changes in cytoplasmic texture cannot be artificially reproduced by manipulating the smoothness of the image or adding irregular large structures.

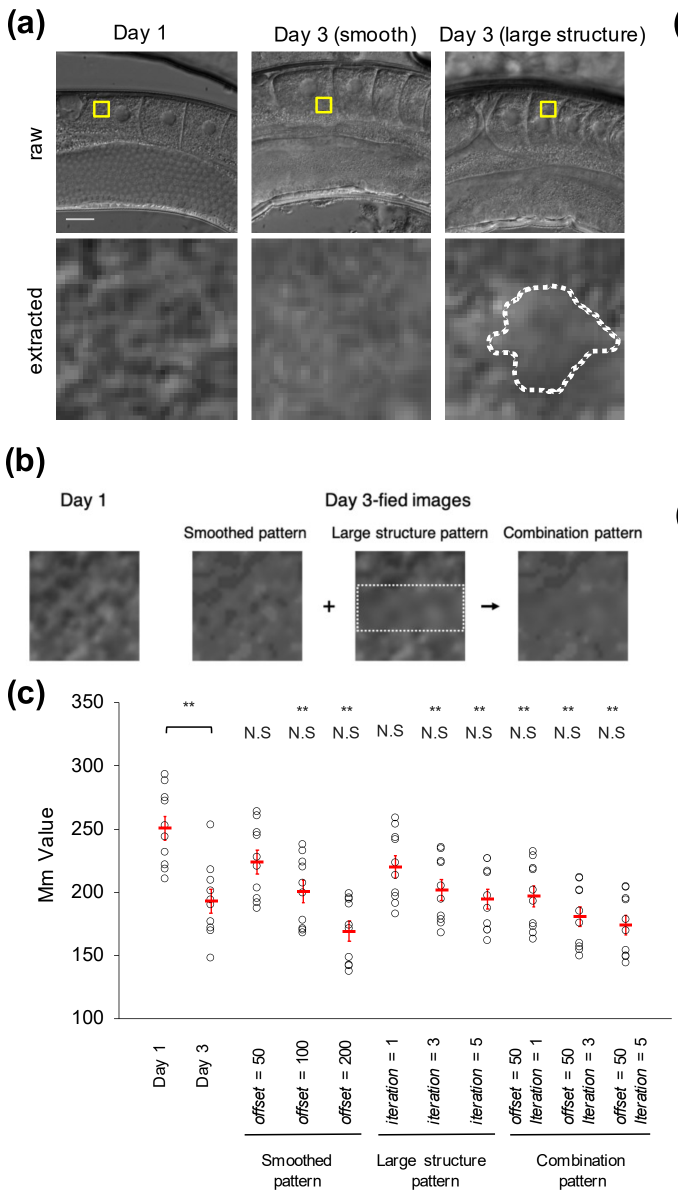

Figure 3.9 Day 3-fied images created from Day 1 images.

(a) Comparison of cytoplasmic texture between Day 1 and Day 3 oocytes. Top, oocyte images; yellow areas indicate representative extracted areas. Scale bar, 20 µm. Bottom, images of the extracted areas. The extracted area of the Day 3 oocyte (middle) appears to have a smoother texture than that of the Day 1 oocyte (left). The extracted area of the Day 3 oocyte (right) contains large structures (marked by a dotted white line), whereas that of the Day 1 oocyte is homogeneous. (b) Extracted areas of a Day 1 image and three Day 3-fied images (left, Smoothed pattern; middle, Large Structure pattern; right, Combination pattern) created from the Day 1 image. The dotted white line indicates the filtered area. (c) Max-min (Mm) Values (3×3-pixel window) of actual Day 1 and actual Day 3 images, and the three patterns of Day 3-fied images. The Smoothed pattern parameter *offset* was set to 50, 100, and 200. The Large Structure pattern parameter *iteration* was set to 1, 3, and 5. The Combination pattern parameters (*offset*, *iteration*) were set to (50, 1), (50, 3), and (50, 5). Circles indicate the Mm Values of individual animals (n = 10 animals in each age group; orientation of the worms is 0 degrees); red bars indicate the mean values. Error bars indicate SEM. Asterisks indicate statistical significance (Tukey–Kramer test) between actual Day 1 and actual Day 3 images or actual Day 1 and Day 3-fied images (**$P < 0.01$); N.S., no significant difference between actual Day 3 and Day 3-fied images. (d and e) Curves of mean *Correlation* (COR) as a function of distance d when $\theta = 135$ are shown for actual Day 1, actual Day 3, and Day 3-fied oocyte images created with (d) Smoothed pattern (*offset* = 50 or 200) or (e) Large Structure pattern (*iteration* = 1 or 5). Data are means ± SEM (n = 10 animals in each age group; orientation of the worms is 0 degrees).

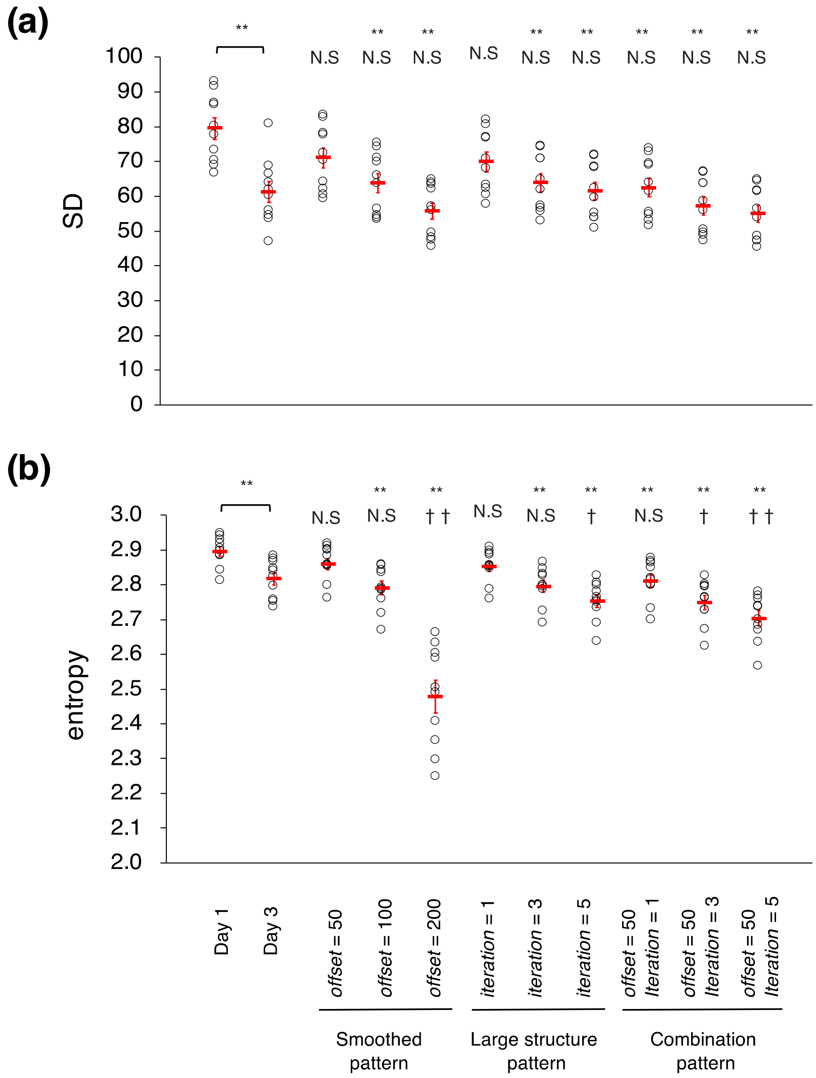

Figure 3.10 Comparison of SD and entropy between actual images and Day 3-fied images.

(a) SD and (b) entropy of actual Day 1, actual Day 3, and the three patterns of Day 3-fied images were calculated using a window size of 3×3-pixels. The Smoothed pattern parameter *offset* was set to 50, 100, and 200. The Large Structure pattern parameter *iteration* was set to 1, 3, and 5. The Combination pattern parameters (*offset*, *iteration*) were set to (50, 1), (50, 3), and (50, 5). Circles indicate the image features of individual animals (n = 10 animals in each age group; orientation of the worms is 0 degrees); red bars indicate the mean values. Error bars indicate SEM. Symbols indicate statistical significance (Tukey–Kramer test) between actual Day1 and actual Day 3 or Day 3-fied images (**$P < 0.01$) or between actual Day 3 and Day 3-fied images (†$P < 0.05$, ††$P < 0.01$); N.S., no significant difference between actual Day 3 and Day 3-fied images.

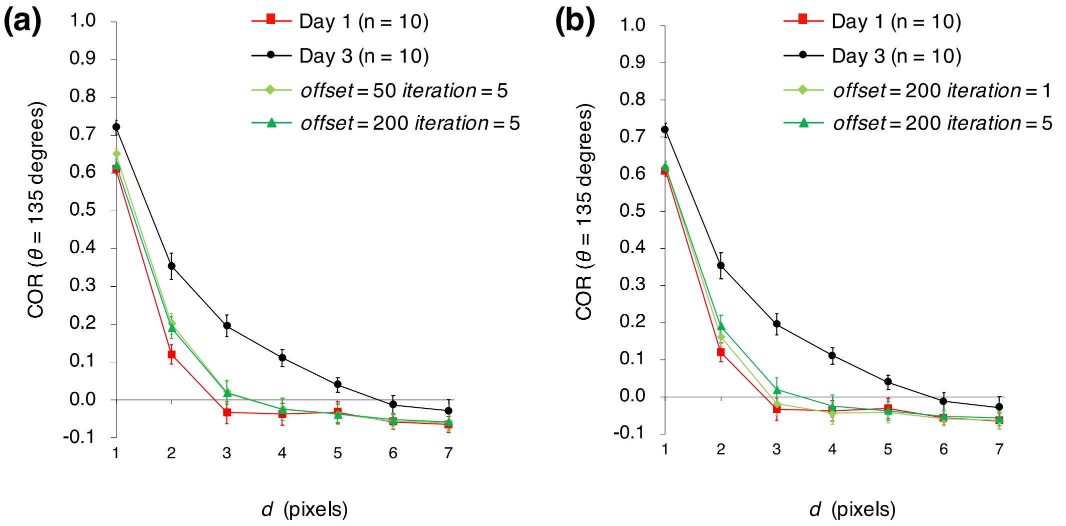

Figure 3.11 *Correlation* calculated for Day 1 and Day 3 oocyte images and Day 3-fied oocyte images with two different Combination patterns.

Curves of mean *Correlation* (COR) as a function of distance d when $\theta = 135$ are shown. Data are means ± SEM (n = 10 animals each age group; orientation of the worms is 0 degrees). The parameters for the Combination pattern (*offset* and *iteration*) were set to (a) (50, 5) and (200, 5) or (b) (200, 1) and (200, 5), respectively.

3.2.6 Synthetic images with different sizes of granules recapitulated the difference in COR between Day 1 and Day 3 oocytes

To investigate what factor causes the d value at which COR converges to zero to differ between Day 1 and Day 3 oocytes, I created simple synthetic images based on two hypotheses: that the (1) number or (2) size of granules in the cytoplasm changes with aging. I therefore evaluated the convergence of COR to zero in the synthetic images with different granule numbers (N) or sizes (R pixels) (Figure 3.12a).

When I varied granule number but kept the granule size constant at $R = 10$, COR in the synthetic images converged to zero at approximately the same d regardless of whether 200 or 150 granules were present (Figure 3.12b). In contrast, when I varied the granule size but kept the granule number constant at $N = 200$, COR converged at a larger d when the granule size was 12 pixels compared with 10 pixels (Figure 3.12c). Therefore, merely altering the number of the granules did not recapitulate the difference in the convergence of COR between Day 1 and Day 3 oocytes, but changing the size of cytoplasmic granules did recapitulate this difference.

To objectively assess whether changing granule size in synthetic images yields the anticipated difference in the d at which COR converges to zero, I exponentially approximated COR curves by using equation (3.1), where a is the amplitude, b is a constant that dictates the d value at which $f(x)$ converges to zero, and c is the offset.

$$f(x) = ae^{-\frac{x}{b}} + c \tag{3.1}$$

In the approximation function, as b increases, the d value at which $f(x)$ converged to zero increases. The difference in the d at which COR converges to zero between Day 1 and Day 3 oocytes should reflect the difference in b values. When I compared the b in the function approximating COR between Day 1 and Day 3 oocytes, the b of Day 3 ($b = 1.7$) was larger than that of Day 1 ($b = 0.7$; Figure 3.12d). Next, I approximated COR of the synthetic images. The difference in b was greater when I manipulated granule size R (Figure 3.12f; $[N, R] = [200, 10]$, $b = 3.0$; $[N, R] = [200, 12]$, $b = 4.7$) than when I varied granule number (N) (Figure 3.12e; $[N, R] = [200, 10]$, $b = 3.0$; $[N, R] = [150, 10]$, $b = 3.4$). The b was larger for the larger granule size than the smaller granule size. These results indicate that the difference of the COR property "d at which COR converges to zero" between Day 1 and Day 3 oocytes can be reproduced by changing the size of the granules.

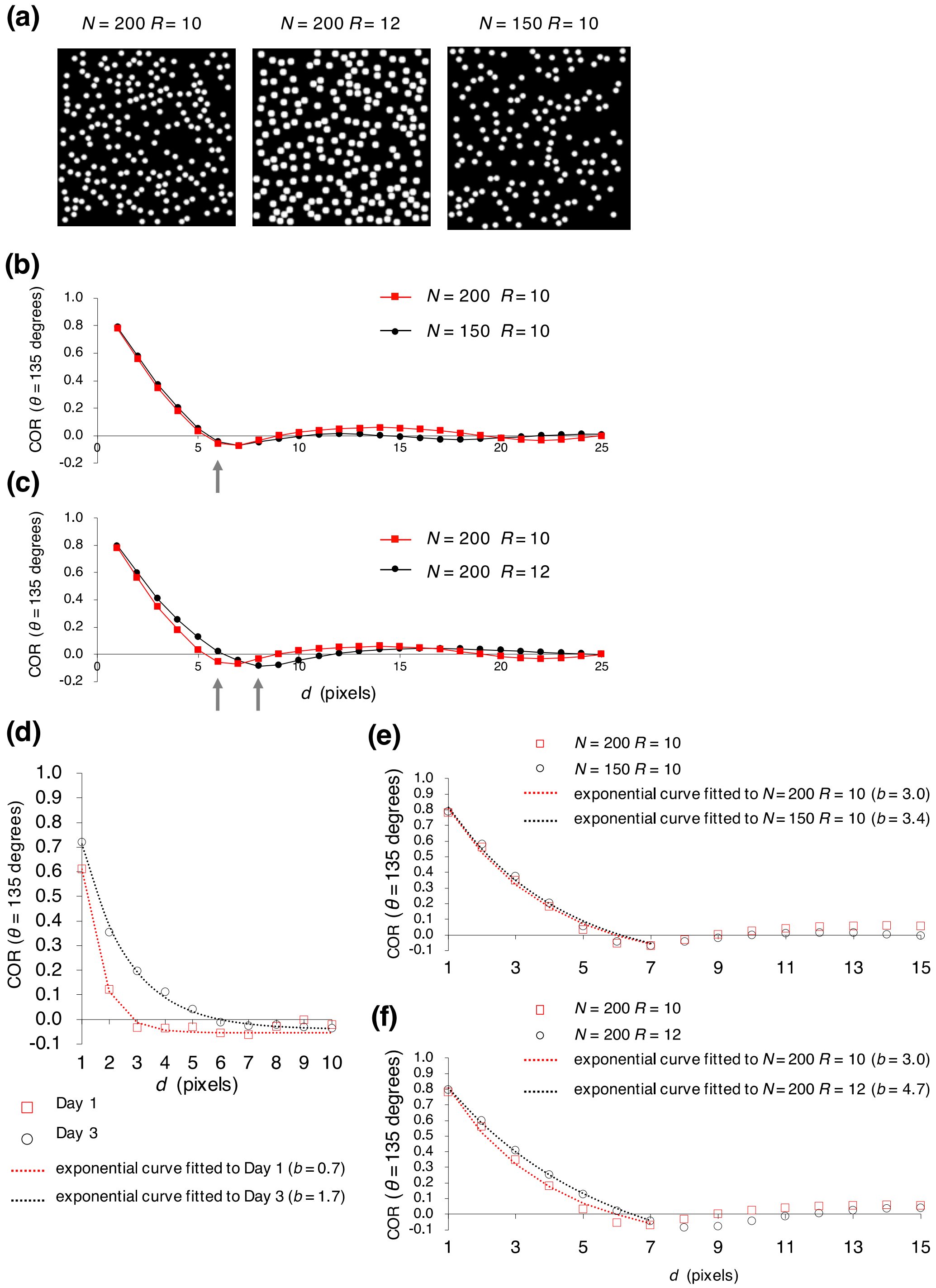

Figure 3.12 Synthetic images created by using different numbers and sizes of particles.

(a) Synthetic images created by setting the number (N) and size (R pixels) of particles to (left) 200 and 10, (middle) 200 and 12, or (right) 150 and 10, respectively. (b and c) Curves of mean *Correlation* (COR) as a function of distance d when $\theta = 135$ are shown for synthetic images with different (b) numbers (N) or (c) sizes (R pixels) of particles. Gray arrows indicate d converging to zero. (d) Exponential curves fitted to COR values as a function of d when $\theta = 135$ are shown for actual Day 1 and Day 3 oocytes (n = 10 animals in each age group; orientation of the worms is 0 degrees). (e and f) Exponential curves fitted to COR values as a function of *d* when $\theta = 135$ are shown for synthetic images with different (e) numbers (N) or (f) sizes (R pixels) of particles.

3.2.7 Granules in *C. elegans* Oocytes are Larger on Day 3 than Day 1

In the synthetic images, changing the granule size reproduced the difference in COR between Day 1 and Day 3 oocytes, suggesting that cytoplasmic granules in *C. elegans* oocytes might change in size with aging. To examine whether granules in DIC images demonstrated age-associated size variation, I manually measured granules and compared their size on Days 1 and 3 (n = 8 animals in each age group; Figure 3.13a). Granules were significantly larger in Day 3 oocytes than Day 1 oocytes (Figure 3.13b).

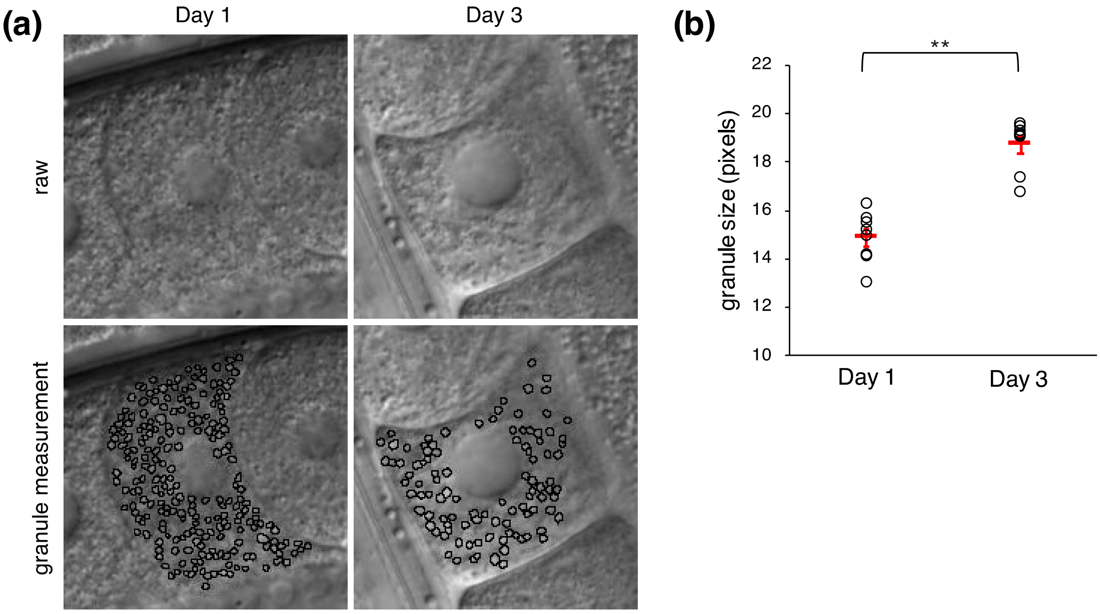

Figure 3.13 Measurement of the size of cytoplasmic granules in differential interference contrast images.

(a) Representative differential interference contrast images of oocytes. Left, Day 1 oocyte. Right, Day 3 oocyte. Top, Raw images. Bottom, Manual detection of granules on raw images. (b) Comparison of the size of granules manually measured in Day 1 and Day 3 oocytes. The sizes of many of the elongated and clustered granules in Day 3 oocytes were not measured. Circles indicate individual animals (n = 8 animals in each age group); red bars indicate the mean value. Error bars indicate SEM. Asterisks indicate statistical significance (**$P < 0.01$; Welch's two-tailed *t* test).

3.3 Discussion

In this study, I found that the texture of the cytoplasm in *C. elegans* oocytes varies with their age. These changes were characterized quantitatively through the DIC image features of Mm Value and COR, the second of which is based on the second-order statistic GLCM. In addition, with the use of appropriate parameter sets, COR characterized these age-associated changes in texture more significantly than Mm Value. Furthermore, analysis of synthetic images and measurement of the size of cytoplasmic granules suggested that the cytoplasmic granules in *C. elegans* oocytes become larger with aging.

Mm Value, a measure of texture roughness, is calculated as the mean of the difference between the maximum and minimum intensities within successive moving windows. The statistical significance of the difference in Mm Values between Day 1 and Day 3 oocytes decreased as the window size increased (Figure 3.2e). If the texture contrast is uniform within an oocyte, calculating Mm Value by using a window size that is smaller than the granule size enables the Mm Value to fluctuate depending on the size or density of granules. However, this variation in the Mm Value cannot occur when the window size used for determining Mm Value might contains multiple granules, such as 13×13, 15×15, or 17×17 pixels. Mm Value for Day 1 oocytes remained significantly larger than that for Day 3 oocytes for these window sizes (P values < 0.05; Figure 3.2e). Therefore, texture contrast might decrease with aging. However, the utility of Mm Value for characterizing the age-associated changes in cytoplasmic texture disappeared when window size was set to 19×19 pixels or larger (all P values > 0.05; Figure 3.2e). When determined by using windows sufficiently large to contain multiple granules, the P values for age-associated differences in Mm Value increased as the window size increased. This may indicate that texture contrast changes in a spatially inhomogeneous manner.

Regardless of window size, the Mm Values of the Day 3-fied images based on the Smoothed pattern were significantly smaller than those of Day 1 images (Figure 3.14a). In addition, the Mm Values of the Day 3 images did not differ significantly from those of Day 1 images when the window was 25×25 pixels or larger. Furthermore, contrast in the Smoothed pattern image was decreased due to normalization to the overall texture contrast throughout the image. Therefore, the results suggest that texture contrast in oocytes does not change homogeneously from Day 1 to Day 3. The relationship between the Mm Values of Day 1 and 3 images may reflect the inhomogeneous changes of the texture contrast. Given that changes in the optical phase gradient can alter contrast in DIC images, the age-associated decrease in texture contrast might reflect a change in granule content due to chemical modification or a difference in content quantity. Similar to the results for Mm Values of Day 3 images, the Mm Values of Day 3-fied images with the Large Structure and Combination patterns were not significantly different from Day 1 images when the window was 25×25 pixels or larger (Figure 3.14b and c). The Day 3-fied images based on the Large Structure and Combination patterns were created by changing the contrast of the Day 1 image in a spatially inhomogeneous manner.

Compared with SD and entropy, the Mm value characterized the age-associated differences in cytoplasmic texture between Day 1 and 3 oocytes for a broader range of window size (Figure 3.2e–g; Figure 3.4). SD and entropy were calculated by using the grey values of all pixels in the moving window, whereas the Mm Value was calculated by using the grey values of only the maximum and minimum intensities in the moving window. The applicability of the Mm Value across many window sizes may stem from the use of these two extreme values.

COR significantly characterized age-associated variations between the Day 1 and Day 3 oocytes when using smaller d but not or less significantly when using larger d (Figure 3.5b–e). This finding suggests some small changes in structure with aging. Therefore, COR likely characterized age-associated changes in texture by recognizing small structures in the cytoplasm.

The d value at which COR converged to zero was larger in Day 3 oocytes than in Day 1 oocytes (Figure 3.5b–e). The d at which COR converged to zero in Day 3-fied images differed markedly from that in actual Day 3 images (Figure 3.9d and e), and the d at which COR converged to zero in the synthetic images was affected by the size of the granules rather than their quantity (Figure 3.12b and c). These results suggest that granule size is the major factor affecting the convergence of COR to zero, and that the difference in the convergence properties of COR between Day 1 and Day 3 images may reflect the larger size of granules in Day 3 oocytes. Supporting this notion, I found that cytoplasmic granules in Day 3 oocytes were significantly larger than those in Day 1 oocytes (Figure 3.13b); i.e., cytoplasmic granules in *C. elegans* oocytes become larger with age.

At the optimal parameter setting ($d = 1, \theta = 135$) and a window of 3×3 pixels, COR characterized cytoplasmic texture with a lower P value than that obtained with the Mm Value. However, COR was not always superior to Mm value because the effectiveness of COR depended on the angle θ and distance d. The results of image analysis of rotated worms suggest that the age-associated differences in texture include an angle-dependent property that is intrinsic to the DIC imaging system. The results of analyzing rescaled images suggest that the age-associated differences also include a size-dependent property intrinsic to the resolution of the imaging system. At appropriate parameters, COR characterized the changes in texture with lower P values than those obtained with Mm Value, but Mm Value was more informative at a broader range of parameters and was not particularly influenced by the angle-dependent property of DIC images. Mm Value may detect a feature of the age-associated changes that COR cannot detect. Further studies are needed to clarify the difference in the characteristics of the age-associated changes detected by Mm Value and COR.

Reported age-associated changes in the morphologic appearance of *C. elegans* oocytes include oocyte shrinkage, loosened contacts, and aggregation into large clusters [18][19]. Here I have quantitatively characterized age-associated changes in the cytoplasmic texture of *C. elegans* oocytes through several statistical image features, such as Mm Value and COR. Cytoplasmic texture would reflect the internal status of oocytes more directly than the external morphologic appearance. Quantitative analysis of cytoplasmic texture and measurement of granules suggest that the cytoplasmic granules in *C. elegans* oocytes become larger with aging. Mm Value and COR can be used as objective methods to quantify age-associated differences in oocyte appearance, which may reflect oocyte fertility. To use the image features to classify the texture of oocytes according to their age, image features should differ markedly relative to oocyte age.

Although Mm value and COR characterized age-associated changes in cytoplasmic texture, their distribution overlapped between age groups, and the values differed significantly between Day 1 and Day 3 oocytes but not between Day 1 and Day 2 oocytes. These results suggest that Mm value and COR may be insufficiently sensitive for accurate recognition and classification of small textural changes. To increase sensitivity, multi-dimensional analysis using additional image features or application of machine learning methods, such as deep learning, may be required. The age-associated changes in cytoplasmic texture can be subtle.

COR was similar on Day 1 and Day 2, and significantly increased on Day 3. Mm value was similar on Day 1 and Day 2, and significantly decreased on Day 3. A possible explanation of these results is that the age-related change in oocyte quality is not reflected in the cytoplasmic texture of oocytes between Day 1 and Day 2. Alternatively, there could be almost no age-related change in the oocyte quality between Day 1 and Day 2. Given that almost all of the fertilized embryos developed successfully in the Day 1 and Day 2 adults, but not the Day 3 adults, it is likely that oocyte quality does not change much between Day 1 and Day 2, but remarkably decreases on Day 3.

Some of the cytoplasmic granules in the DIC texture images may be yolk granules [71][72]. Yolk is a lipoprotein composed of lipids and lipid-binding proteins called vitellogenins [73]. In *C. elegans*, vitellogenins are synthesized in the intestine and transported into maturing oocytes through endocytosis [74][75]. Yolk provides essential nutrients to the eggs to support embryonic development [75]. During reproductive senescence, the intestine continues to produce and secrete large amounts of yolk protein. In adult *C. elegans* hermaphrodites, yolk accumulates towards the end of the self-fertile reproductive period [76][77]. Provisioning of vitellogenin to embryos increases with maternal age [78] and might increase the lipid content in embryos and oocytes, given that vitellogenins transport lipids into embryos [73][78]. Taking these findings together with my data, I propose that the cytoplasmic granules in aged adults (Day 3 and later) might enlarge due to an increase in vitellogenin content or in vitellogenin-transported embryonic lipid content.

What is the relationship between decreased fertility and yolk accumulation with aging? Yolk accumulation may contribute to the decrease in fertility. High levels of yolk appear to be detrimental and decrease the lifespan of *C. elegans* [79]. In contrast, knockdown of vitellogenin expression extends lifespan [80][81]. Increased amounts of yolk might accelerate the aging of oocytes or animals, resulting in decreased fertility. Alternatively, decreased oocyte fertility might contribute to yolk accumulation. Moreover, I cannot exclude the possibility that yolk accumulation does not affect fertility directly. Further experiments are needed to clarify the relationship between yolk levels and fertility in this and other species.

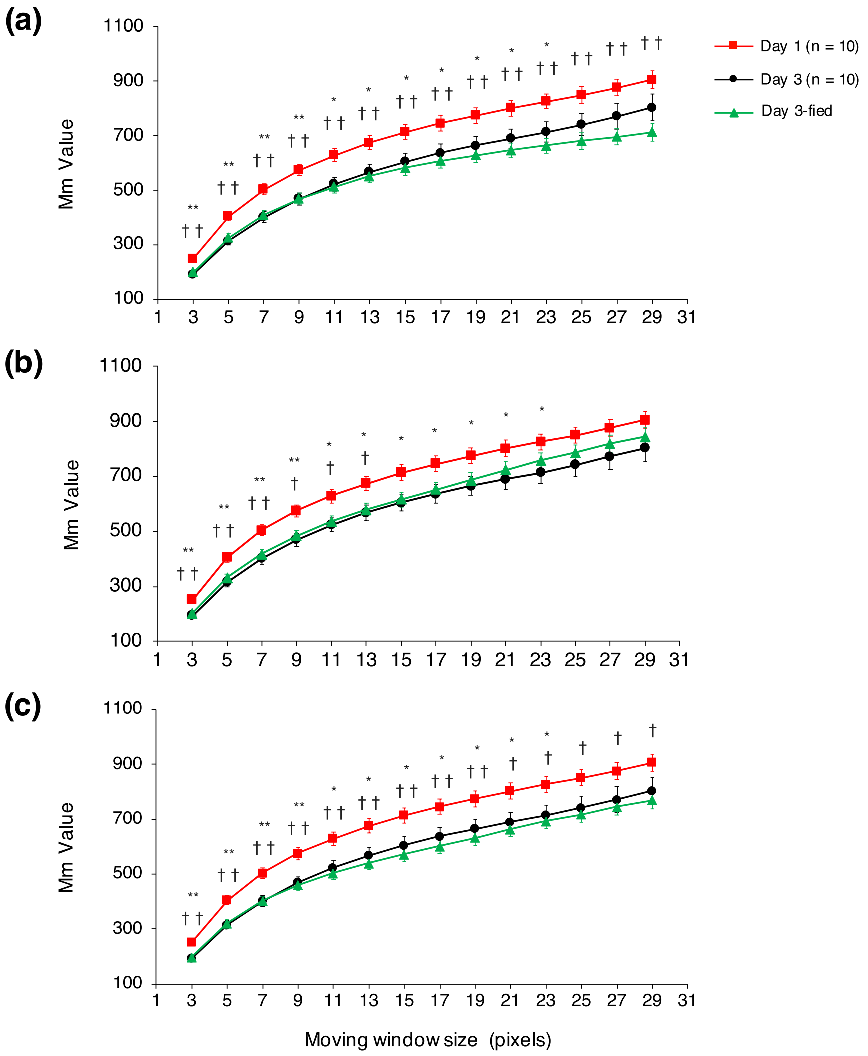

Figure 3.14 Comparison of Max-min Values between actual Day 1, actual Day 3, and Day 3-fied oocyte images for various window sizes from 3×3 to 29×29 pixels.

Data are means ± SEM (n = 10 animals each age group; orientation of the worms is 0 degrees) (a) Day3-fied images were created with Smoothed pattern (*offset* was set to 100). (b) Day3-fied images were created with Large Structure pattern (*iteration* was set to 3). (c) Day3-fied images were created with Combination pattern [(*offset*, *iteration*) were set to (50, 1)]. Symbols indicate statistical significance (Tukey–Kramer test) between Day 1 and Day 3 images (*$P < 0.05$, **$P < 0.01$) or Day 1 and Day 3-fied images (†$P < 0.05$, ††$P < 0.01$).

3.4 Methods

3.4.1 *C. elegans* Strains and Growth Conditions

Caenorhabditis elegans (Bristol N2 strain) were grown under standard conditions [23]. The L4 larval stage was considered as Day 0; worms were defined as Day 1, Day 2, and Day 3 adults at 18–24 h, 43–46 h, and 67–70 h after L4, respectively. This experiment was done by Hatsumi Okada (H.O.) in Laboratory for Developmental Dynamics at RIKEN Center for Biosystems Dynamics Research.

3.4.2 Imaging of Oocytes

Worms were immobilized in a polystyrene nanoparticle suspension [82] supplemented with 5-hydroxytryptamine [83] on agarose pads. The anterior gonad was observed by Nomarski DIC microscopy with the use of a Leica HCX PL APO 63×/1.20 W CORR objective and an iXonX3 electron-multiplying CCD camera controlled with live-cell imaging software (Andor iQ). The plane of focus was through the oocyte nucleus. Images of nematodes at four angles (0, 45, 90, and 135 degrees) were obtained by rotating the Day 1 samples; 0 degrees was defined as horizontal orientation. Digital images of 512×512 pixels were converted to 14-bit TIFF format (0.25 µm per pixel). The images were captured by H.O.

3.4.3 Calculation of Image Features

To calculate image features, random regions of 30×30 pixels were extracted from the cytoplasm, without including nuclei or cell boundaries. The three oocytes most proximal to the spermatheca in the anterior gonad were used for each animal, and one region was extracted from each oocyte. Image features of individual animals were defined as the mean of those in the extracted three regions.

The first-order statistical features Mm Value, SD, and entropy were calculated by moving the local window within the confines of the border of the extracted region. SD was defined as the mean of the standard deviations of the pixel intensities in the moving window. Entropy was defined as the mean of entropies (calculated according to the following the equation) in the moving window:

$$-\sum_{k=0}^{\mathrm{G}-1} P(k)\log_2 P(k),$$

where G is the number of gray levels, and $P(k)$ is the probability of occurrence of gray level k in the moving window.

Second-order statistical features based on GLCM—*Correlation* (COR), *Angular Second Moment* (ASM), *Contrast* (CON), *Inverse Difference Moment* (IDM), and *Entropy* (ENT)—were calculated by using the following equations and the co-occurrence matrix $P(i, j \mid d, \theta)$:

$$\mathrm{COR} = \frac{\sum_{i=0}^{\mathrm{G}-1} \sum_{j=0}^{\mathrm{G}-1} ijP(i,j) \; - \; \mu_x\mu_y}{\sigma_x\sigma_y}$$

$$\mathrm{ASM} = \sum_{i=0}^{\mathrm{G}-1} \sum_{j=0}^{\mathrm{G}-1} \{P(i,j)\}^2$$

$$\mathrm{CON} \; = \sum_{i=0}^{\mathrm{G}-1} \sum_{j=0}^{\mathrm{G}-1} (i-j)^2 P(i,j)$$

$$\mathrm{IDM} \; = \sum_{i=0}^{\mathrm{G}-1} \sum_{j=0}^{\mathrm{G}-1} \frac{P(i,j)}{1+(i-j)^2}, \text{ and}$$

$$\mathrm{ENT} = -\sum_{i=0}^{\mathrm{G}-1} \sum_{j=0}^{\mathrm{G}-1} P(i,j) \log\big(P(i,j)\big),$$

where μ_x, μ_y, σ_x, and σ_y are the means and standard deviations in the x and y direction given by

$$\mu_x = \sum_{i=0}^{\mathrm{G}-1} \sum_{j=0}^{\mathrm{G}-1} iP(i,j)\,, \; \mu_y = \sum_{i=0}^{\mathrm{G}-1} \sum_{j=0}^{\mathrm{G}-1} jP(i,j) \text{ and}$$

$${\sigma_x}^2 = \sum_{i=0}^{\mathrm{G}-1} \sum_{j=0}^{\mathrm{G}-1} P(i,j)\,(i-\mu_x)^2\,, \; {\sigma_y}^2 = \sum_{i=0}^{\mathrm{G}-1} \sum_{j=0}^{\mathrm{G}-1} P(i,j)\,\left(j-\mu_y\right)^2.$$

$P(i, j \mid d, \theta)$ was defined as symmetric (see Figure 3.5a).

3.4.4 Computational Complexity

The computational complexity of the Mm Value is of the order of $O(\mathrm{W}^2\mathrm{M}^2)$, where W is the window size, and M is the size of the input image. The computational complexity of the COR is divided into two components: (1) creating the GLCM and (2) calculating the COR from the GLCM [84]; the computational complexity is of the order of $O(\mathrm{L}^2)+O(\mathrm{G}^2)$, where L is the length of the neighborhood window in GLCM feature extraction, and G is the number of grey levels of the input image. Using my codes, it takes about 0.5×10^{-3} s per image to calculate the Mm Value for W = 3 pixels and M = 30 pixels on my PC (Intel® Core™ i5, 1.6 GHz). The calculation of the COR for L = 1 pixel and G = 256 takes about 2.4×10^{-3} s per image on my PC (Table 3.1).

Table 3.1 The processing time per image for Max-min Value, SD, entropy and *Correlation*

The processing time was measured for input images of various sizes. The parameter settings were changed according to the image size. Processing time per image was calculated by averaging the processing time of 1000 images. The processing time for Max-min Value (Mm Value) was equivalent to that for SD, and that for entropy was greater than that for MmValue or SD. The computational complexities of the SD and entropy are of the order of $O(W^2M^2)$ and $O(W^2M^2)+O(GM^2)$, respectively, where W is the window size, M is the size of the input image and G is the number of grey levels of the input image. The processing time for the first-order statistical features was less than that for COR when the input images were small (30×30 pixels), but greater than that for *Correlation* (COR) when the input images were large (150×150 pixels). This was because the processing times for the first-order statistical features increased with the image size, but the processing time for COR was largely unaffected by the image size.

Size of input image (pixels)	Window size (pixels) for Mm Value, SD, and entropy	Distance parameter (pixels) for COR	Processing time per image (s)			
			Mm Value	SD	entropy	COR (θ = 135 deg)
30×30	3	1	0.5×10^{-3}	0.5×10^{-3}	1.0×10^{-3}	2.4×10^{-3}
60×60	5	2	0.6×10^{-3}	0.7×10^{-3}	3.4×10^{-3}	2.3×10^{-3}
150×150	11	5	1.2×10^{-2}	1.1×10^{-2}	2.8×10^{-2}	2.3×10^{-3}

3.4.5 Creation of the Rescaled Images

The images were rescaled using bilinear interpolation. I used data from worms oriented at 0 degrees (n = 10 animals) as the original images (30×30 pixels). To halve the resolution of the original images, the images were downscaled to 15×15 pixels. To double the resolution of the original images, the images were upscaled to 60×60 pixels.

3.4.6 Creation of the Synthetic Images

Synthetic images were created by randomly locating N white granules with diameter R pixels on a black background image of 300×300 pixels. Granules could not overlap or protrude from the border of the image.

3.4.7 Fitting Equations to the COR Curves

To fit equations to the COR datasets (actual Day 1 and Day 3 images, and synthetic images), I performed nonlinear regression analyses using the exponential function described in the Results section:

$$f(x) = ae^{-\frac{x}{b}} + c\,.$$

I used the COR data for d of 1 to 7 pixels to estimate the curve for convergence of COR to zero. I used data from worms oriented to 0 degrees (n = 10 animals).

3.4.8 Quantification of the Granule Size

For each worm, I manually measured the cytoplasmic granules in the oocyte that was second-most proximal to the spermatheca. Granules were determined as non-overlapping circular or nearly circular regions where signal intensity exceeded the background intensity. Many of the elongated and clustered granules in Day 3 oocytes were not measured.

3.4.9 Statistical Analyses

Statistical analyses were performed using R software. *P* values for pair-wise comparisons of data sets were calculated using Welch's two-tailed *t* test. Those for multiple comparisons of data sets were calculated using Tukey–Kramer test.

Chapter 4

Texture-based Screening of Genes Involved in Reproductive Aging

4.1 Introduction

Reproductive ability declines with aging, thereby increasing errors in fertilization, chromosome segregation, and embryonic cleavage [6][32][33]. However, the mechanisms regulating reproductive aging remain incompletely understood.

Caenorhabditis elegans (*C. elegans*) is a leading model for studying aging because of its short lifespan (~ 3 weeks) and the evolutionary conservation of longevity pathways from *C. elegans* to humans [28]. In particular, *C. elegans* has been developed as a model for studying age-related decline in fertility [18].

Age-related changes in oocytes are found not only in its function but also in appearance [18][19][33]. I showed that the texture of the cytoplasm in *C. elegans* oocytes varies with age [85] (explained in Chapter 3). I quantitatively characterized this change through the differential interference contrast (DIC) image features of Max-min Value (Mm Value) and *Correlation* (COR), which is based on Gray Level Co-occurrence Matrix (GLCM) [66] (Figure 4.1a and b; explained in Chapter 3). Mm Value is a contrast feature that is calculated as the mean of the difference between the maximum and minimum intensities within successive moving windows. The Mm Value in the cytoplasmic texture of oocytes decreases with aging while the COR, at several levels of parameters, increased with aging [85] (explained in Chapter 3). However, how variances in texture are related to biological and genetic process has not been clarified. Genes whose knockdown causes the texture changes as seen in the oocytes with aging are considered to be candidate genes involved in the aging pathway. The identification of candidate genes involved in the aging pathway may lead to understanding of the mechanisms underlying oocyte aging.

Worm Developmental Dynamics Database 2 (WDDD2; https://wddd.riken.jp) is an update of WDDD [86]. It shares four-dimensional DIC microscopy images of 33 wild-type and 1728 RNA interference (RNAi)-treated *C. elegans* embryos. RNAi is a phenomenon in which specific genes are inactivated by introduction of double-stranded RNA with complementary sequences [26]. The RNAi-treated embryos correspond to the 316 essential embryonic genes that exhibited an embryonic lethal phenotype in 100% of offspring when silenced in the previous genome-wide screen [87].

RNAi screening using computational image processing or automatic screening system is one of the state-of-the-art technologies in biomedical research [88][89]. RNAi screening based on morphological features from image processing is unbiased and high-throughput approach. Recently, I proposed a method to quantify the age-associated changes in the cytoplasmic texture of *C. elegans* oocytes [85] (explained in Chapter 3). This method provides a new opportunity to apply the computational image processing-based RNAi screening to studies of aging in *C. elegans* oocytes.

Here, to examine whether gene knockdown can decrease the Mm Value or increase the COR (as seen in oocytes with aging), I analyzed the cytoplasmic texture in the early embryo images in WDDD2. Morphological defects in oocytes correlate with a decreased embryo-hatching rate [18][19]. I assumed that the cytoplasmic texture properties in the oocytes are reflected in the early embryo and screened for genes whose knockdown decreased the Mm Value or increased the COR in cytoplasmic regions of early embryos. I identified five genes whose knockdown resulted in a decreased Mm Value, and one gene whose knockdown led to increased COR, suggesting that the genes are involved in reproductive aging.

4.2 Results

4.2.1 Overview of the Experiments

To identify genes whose expression might affect Mm Values and/or the COR in aging oocytes, I examined the differences in image features between RNAi-treated and wild-type embryos in WDDD2 (Figure 4.1c). I used 33 datasets from wild-type embryos and 1728 datasets from RNAi experiments, where 316 embryonic essential genes were individually silenced.

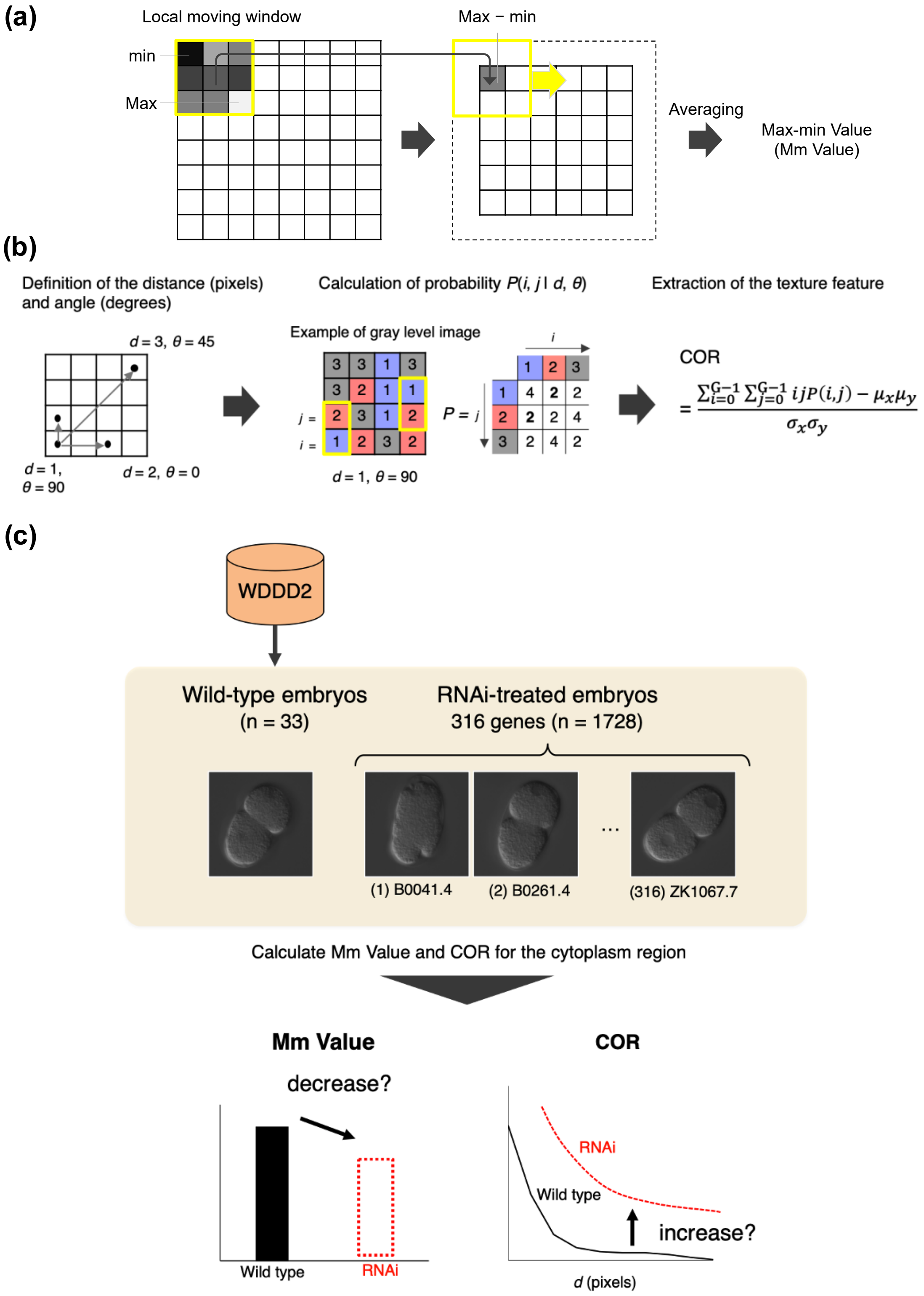

Figure 4.1 Schema of image analysis methodologies.

(a) Algorithm for calculating the Max-min Value (Mm Value). (b) Algorithm for calculating the Gray Level Co-occurrence Matrix (GLCM). When the distance is 1 pixel and the direction is 90 degrees, the calculated number of pixels with $i = 1$ and $j = 2$ or $i = 2$ and $j = 1$ is 2. (c) Overview of our in silico experiments. The labels under the images refer to the individual genes. We screened for genes whose knockdown decreased the Mm Value or increased the COR in cytoplasmic regions of early embryos.

4.2.2 RNAi Screening using the Mm Value

Of the 316 genes tested, I detected five genes, F35G12.8 (*smc-4*), F10C2.4, T09B4.9 (*tin-44*), C29E4.8 (*let-754*) and K05C4.6 (*hmp-2*), whose knockdown significantly reduced the Mm Value compared with that of the wild type (Figure 4.2), suggesting that they are involved in reproductive aging. No genes were found to significantly increase the Mm Value compared with that of wild type.

The *smc-4* gene encodes an ortholog of human SMC4 (structural maintenance of chromosomes 4) protein, a mitotic condensing subunit that acts with MIX-1 to enable chromosome segregation [90]. Chromosomal abnormalities are a major cause of age-related decline in oocyte quality [6]. In *C. elegans* mutants of the TGF-β Sma/Mab pathway, reproductive aging is delayed [91]. The *smc-4* gene is upregulated in the TGF-β mutant oocytes [19]. The condensin SMC declines in both mouse and human oocytes with aging [92][93], suggesting that chromosome segregation is a key process determining oocyte quality that is conserved between worms and mammals [19]. Knockdown of *smc-4* degrades germline and oocyte morphology and increases the rate of unfertilized oocytes and unhatched embryos [19]. In WDDD2, almost all *smc-4* RNAi worms exhibited embryonic lethality and some of them produced unfertilized oocytes.

The F10C2.4 gene encodes the DNA polymerase delta complex subunit and is required for normal chromosome segregation [94]. Reduced expression of this gene may affect reproductive aging due to chromosome segregation errors, similar to *smc-4*.

The *tin-44* gene functions in transporting proteins into the inner mitochondrial membrane and matrix [95][96]. Mitochondria have a pivotal role not only in energy metabolism but also in regulation of the rate of aging [97]. *tin-44* RNAi worms exhibited a shorter lifespan than wild type [98], suggesting that mitochondrial dysfunction caused by RNAi of *tin-44* possibly affects aging.

The genes *let-754* encodes adenylate kinase [99][100] and *hmp-2* encodes β-catenin and is required for proper cell migration [101]. Neither protein has been directly linked to aging. The genes *let-754* and *hmp-2* may be related to the aging pathway or may cause abnormalities in cytoplasmic textures via alternative pathways.

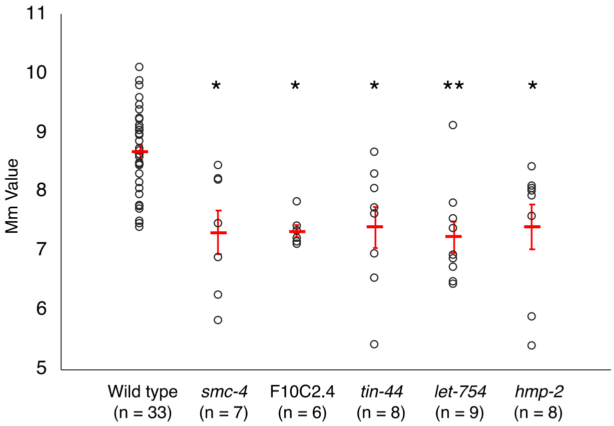

Figure 4.2 Genes identified using the Max-min Value.

When the five genes displayed were silenced in *Caenorhabditis elegans* embryos, the cytoplasmic region showed a significantly lower Max-min Value (Mm Value) than was seen in wild-type embryos. Red bars indicate mean values; error bars indicate SEM. Asterisks indicate statistical significance versus wild type (*$P < 0.05$, **$P < 0.01$; Dunnett's test).

4.2.3 Interaction among the Candidate Genes Screened by the Mm Value

I then automatically predicted the interactions (genetic interactions, co-expression, and physical interactions) among all five gene candidates identified by the Mm Value by using GeneMania software (http://www.genemania.org) [102]. In particular, I examined whether *let-754* and *hmp-2* interact with the three candidate genes that have known age-related functions (i.e., *smc-4*, F10C2.4, *tin-44*). From the network shown in Figure 4.3, three genes, *hcp-3*, *zfp-1*, and *mut-7* have predicted simultaneous interactions with *smc-4*, F10C2.4, and *hmp-2*. Although *tin-44* was predicted to interact with *hmp-2* via two genes, the interaction was relatively weak. I found no association between *let-754* and the genes identified by the Mm Value. The results suggest that *smc-4*, F10C2.4, and *hmp-2* have high genetic interactions and *tin-44* and *let-754* have less interactions with other genes.

I then examined whether the knockdown of the five candidate genes shares any of the phenotype categories annotated by Piano *et al* [103], which are available in the RNAi Database (http://www.rnai.org) [104]. I focused on cytoplasmic phenotypes and found that knockdown of *sm*c-4, F10C2.4, and *hmp-2* was included in the category "Multiple cavities", which is described as "multiple vesicles, vacuoles, or cavities are seen during early embryogenesis". Both the shared phenotype category and the predicted gene interactions mentioned above suggest that *smc-4*, F10C2.4, and *hmp-2* have similar properties in terms of function and phenotype; therefore, *hmp-2* may function in an aging pathway related to chromosome segregation like *smc-4* and F10C2.4. In addition, out of the 27 genes in the "Multiple cavities" category, 13 genes were not included in WDDD2. These 13 genes might include gene(s) whose knockdown decreases Mm Value and have a related function to *smc-4*, F10C2.4, and *hmp-2*.

The five genes whose knockdown reduced the Mm Value can be divided into three groups: a chromosome abnormality group (*smc-4*, F10C2.4, and *hmp-2*), mitochondrial function group (*tin-44*), and unknown group (*let-754*), based on the results of the gene interaction and phenotype category analyses. Therefore, multiple pathways may contribute to reductions in Mm Value.

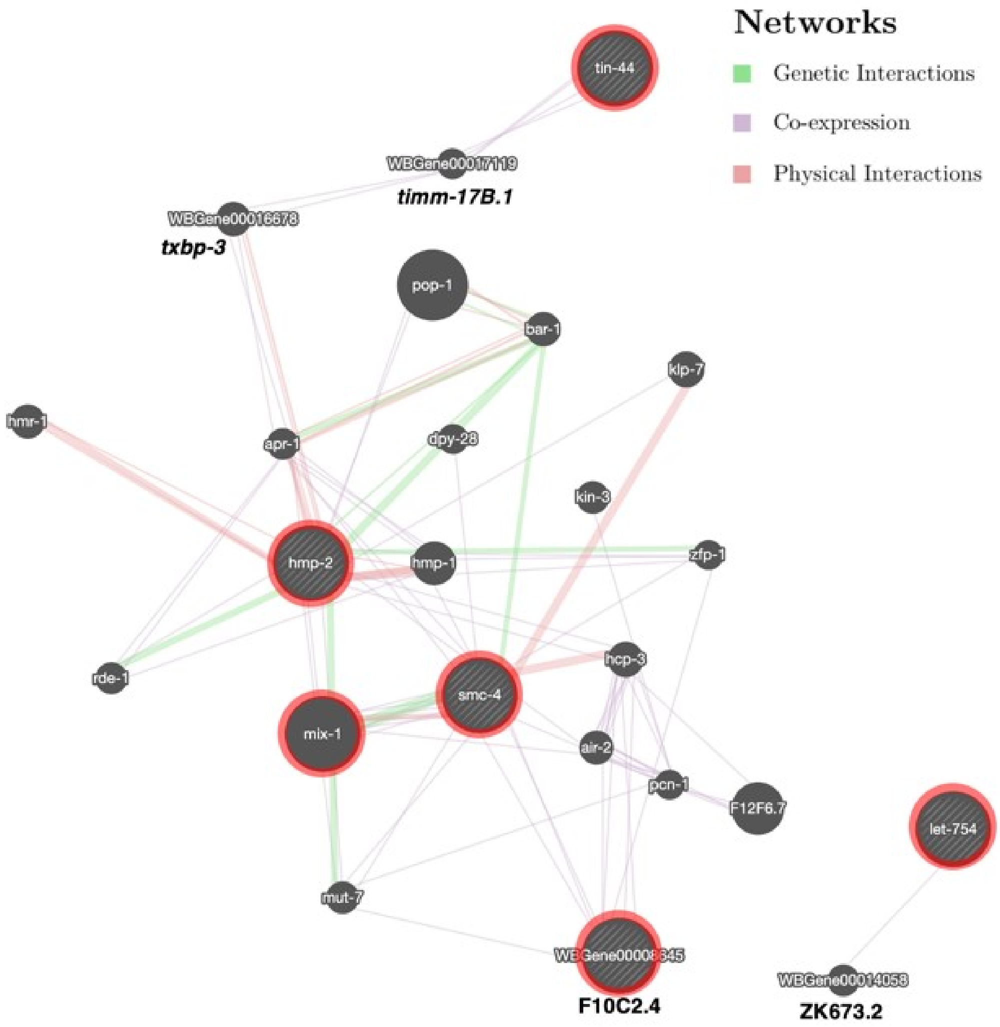

Figure 4.3 Gene interactions among the genes whose knockdown decreased the Max-min Value.

The genes identified by changes in Max-min Value are highlighted by red circles.

4.2.4 RNAi Screening using the COR

I then screened the RNAi-treated embryos' images in WDDD2 to find RNAi-treated embryos whose cytoplasmic regions displayed significantly higher COR than in wild type. The angle parameter of GLCM was set to $\theta = 0, 45, 90$, and 135 degrees. For the 316 genes tested, the COR when the angle was set to 0, 45, or 135 degrees did not differ significantly between RNAi and wild-type embryos. However, for two genes, *csr-1* and *gbp-1*, knockdown significantly increased and decreased the COR, respectively, compared with wild type when θ =90 (Figure 4.4).

The *csr-1* gene encodes CSR-1, an Argonaute protein that is essential for chromosome segregation and embryo viability [105]. CSR-1 is a core component of P granules and acts with P granules to maintain germline integrity [106]. Because the COR increased when *csr-1* was silenced, *csr-1* is a candidate for involvement in oocyte aging.

Conversely, knockdown of *gpb-1* decreased the COR. The *gpb-1* gene encodes the heterotrimeric G protein β subunit, which is required for proper spindle orientation and regulation of egg laying [107][108], but has not yet been shown to be directly related to reproductive aging. Further experiments are needed to clarify the associations between the decline of the COR and gene functions.

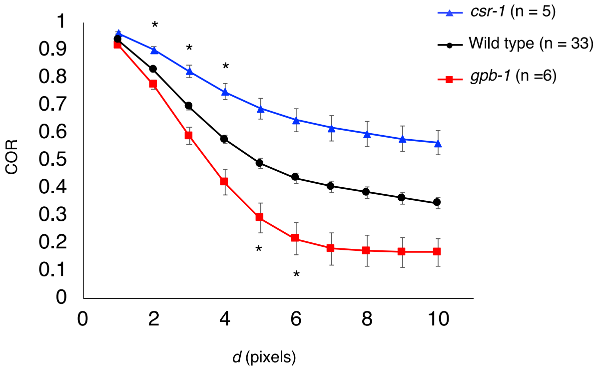

Figure 4.4 Genes identified using the *Correlation*.

Correlation (COR) is displayed as a function of distance *d* for two genes whose knockdown resulted in significantly increased or decreased COR compared with wild type. Error bars indicate SEM. Asterisks indicate statistical significance between the RNA interference embryos and wild-type embryos (*$P < 0.05$, Dunnett's test).

4.3 Discussion

By screening images of RNAi-treaded embryos in WDDD2, I identified genes whose knockdown changes the cytoplasmic texture in early *C. elegans* embryos, mirroring the changes in oocytes with aging. Of 316 target genes, knockdown of five genes was found to significantly decrease the Mm Value and knockdown of one gene significantly increased the COR. These genes could potentially be involved in reproductive aging.

In Chapter 3, the Mm Value and the COR in oocytes changed simultaneously with aging [85]. However, in the current experiment, knockdown of specific genes changed the image features independently, suggesting that the image features can be used to characterize different properties of the age-associated changes in the cytoplasmic texture. In other words, texture changes caused by RNAi knockdown can be divided into two patterns, one that decreases the Mm Value and one that increases the COR, and the associated genes might function in different pathways involved in aging. The insulin/insulin-like growth factor pathway, a well-known pathway controlling the lifespan of *C. elegans*, and the TGF-β Sma/Mab pathway are considered to regulate reproductive lifespan independently [56][91][109]. My results show that knockdown of *smc-4*, which functions in the TGF-β Sma/Mab pathway, decreased the Mm Value in cytoplasmic regions of *C. elegans* embryos, implying that the texture characterized by the Mm Value is involved in the TGF-β pathway. In contrast, the texture characterized by the COR is possibly involved in the insulin/insulin-like growth factor pathway although there is no direct experimental evidence to support this. The texture characterized by the Mm Value reflects the changing contrast in the DIC granules, which may be due to chemical modification or a difference in content quantity of the granules. A change in the COR reflects a change in the size of cytoplasmic granules [85] (explained in Chapter 3). Further experiments are needed to understand the association between gene function and the morphology of the cytoplasmic granules. Elucidation of this association may be helpful for understanding the aging pathways and mechanisms.

4.4 Methods

4.4.1 WDDD 2

Four-dimensional DIC microscope images in the WDDD2 (https://wddd.riken.jp) were recorded in multiple focal planes and at multiple time points (0.10 µm per pixel). In the RNAi screen, young adult worms were separately injected with each double-stranded RNA, and embryos were dissected from the worms immediately after fertilization.

4.4.2 Calculation of Image Features

I used the images at the first time point in embryo development in WDDD2 and at the focal planes where the Mm Value in the entire image was maximum. To detect the cytoplasmic region, I used local image entropy [110]. To calculate image features, random regions of 80×80 pixels were extracted from the cytoplasmic region. Image features of individual embryos were defined as the mean of those in the extracted four regions.

The Mm Value was calculated by moving the local window except for the border in the same way as Chapter 3 [85]. I set the size of the moving window to 3×3 pixels. COR, a second-order statistical feature based on GLCM, was calculated in the same way as Chapter 3.

Chapter 5

Improvement and Evaluation of a Mathematical Model for Fertilization Calcium Wave

5.1 Introduction

Ca^{2+} waves (increase in calcium ion concentration) propagate through the oocyte during fertilization [8]. They trigger several processes such as resumption of meiosis, release of surface granules, and formation of the pronucleus, which are collectively called oocyte activation, and initiate embryonic development [9]. Ca^{2+} waves are found in almost all animal species and are caused by Ca^{2+} channels called inositol 1, 4, 5-trisphosphate receptors on the endoplasmic reticulum, which functions as an intracellular Ca^{2+} store [9][10]. Ca^{2+}-induced Ca^{2+}-release (CICR) is a mechanism of Ca^{2+} wave formation [46]. In CICR, a local increase in Ca^{2+} concentration induces a release of Ca^{2+} from the endoplasmic reticulum, resulting in recurrent releases, which form waves. The spatiotemporal patterns of Ca^{2+} waves differ among animal species and seem to be related to oocyte activation [9]. However, the mechanisms of wave pattern generation are poorly understood.

Takayama and Onami quantified Ca^{2+} wave during fertilization in the nematode *Caenorhabditis elegans* (*C. elegans*), one of the simplest model animals, by using high-speed imaging and image analysis [22]. These animals are easy to observe because their body is transparent, and are easy to manipulate experimentally. They showed that Ca^{2+} wave have two phases: a rapid local rise and a slow global wave. The Ca^{2+} concentration decreases to the basal level after reaching its peak. The fertilized oocyte shows a single Ca^{2+} response [22]. They also performed a simulation using the Nagumo model that assumed CICR and a high initial Ca^{2+} concentration (local rise) in a restricted region. The model produced a biphasic waveform similar to the observed one [22][111], but could not represent the observed gradual decrease in maximum Ca^{2+} concentration with increasing distance from the point of sperm entry. In this study, I propose an improved model that satisfies both conditions of formation of a biphasic wave and the decrease in maximum concentration depending on the position in the oocyte.

5.2 Results

5.2.1 Proposed Model

In the current study, I propose a modified Nagumo model, a reaction–diffusion model that proposed previously [22][111]. In general, a reaction–diffusion equation for the concentration variable c in one-dimensional space is the following equation (5.1), where D is the diffusion coefficient, t is the time variable, and x is the space variable.

$$\frac{\partial c}{\partial t} = D\frac{\partial^2 c}{\partial x^2} + f(c) \tag{5.1}$$

The Nagumo model adopts a cubic polynomial function of c for its reaction term, as expressed in equation (5.2). The Nagumo model is also known as a bistable equation because its reaction term has two stable points at $c = 0$ and 1 [111].

$$f(c) = Ac(1-c)(c-\alpha) \tag{5.2}$$

The parameters in the reaction term, α and A, can be regarded as the threshold at which the endoplasmic reticulum releases Ca^{2+} and as a coefficient regarding the speed of this release, respectively. The maximum $[Ca^{2+}]_{exp}$ values decreased with increasing distance from the point of sperm entry (Figure 5.1c), whereas the maximum $[Ca^{2+}]_{sim}$ values were constant irrespective of the distance (Figure 5.2). The constancy could be due to the reaction term of the Nagumo model, in which convergence values are independent of the space variable x.

To solve the qualitative inconsistency between the experimental and simulated results, I modified the Nagumo model by introducing c_{max}, a linear monotonically decreasing function of x instead of the constant 1. With c_{max}, the convergence values are expected to decrease with increasing distance from the point of sperm entry. The c_{max} function was obtained by applying the least squares method to the maximum Ca^{2+} concentration in each region of interest (ROI), which is calculated from the experimental data (Figure 5.3), resulting in equation (5.4). The maximum concentrations were then calibrated to c (0–1).

$$\frac{\partial c}{\partial t} = D\frac{\partial^2 c}{\partial x^2} + Ac(c_{max}-c)(c-\alpha) \tag{5.3}$$

$$c_{max} = -0.00990\,x + 0.882 \tag{5.4}$$

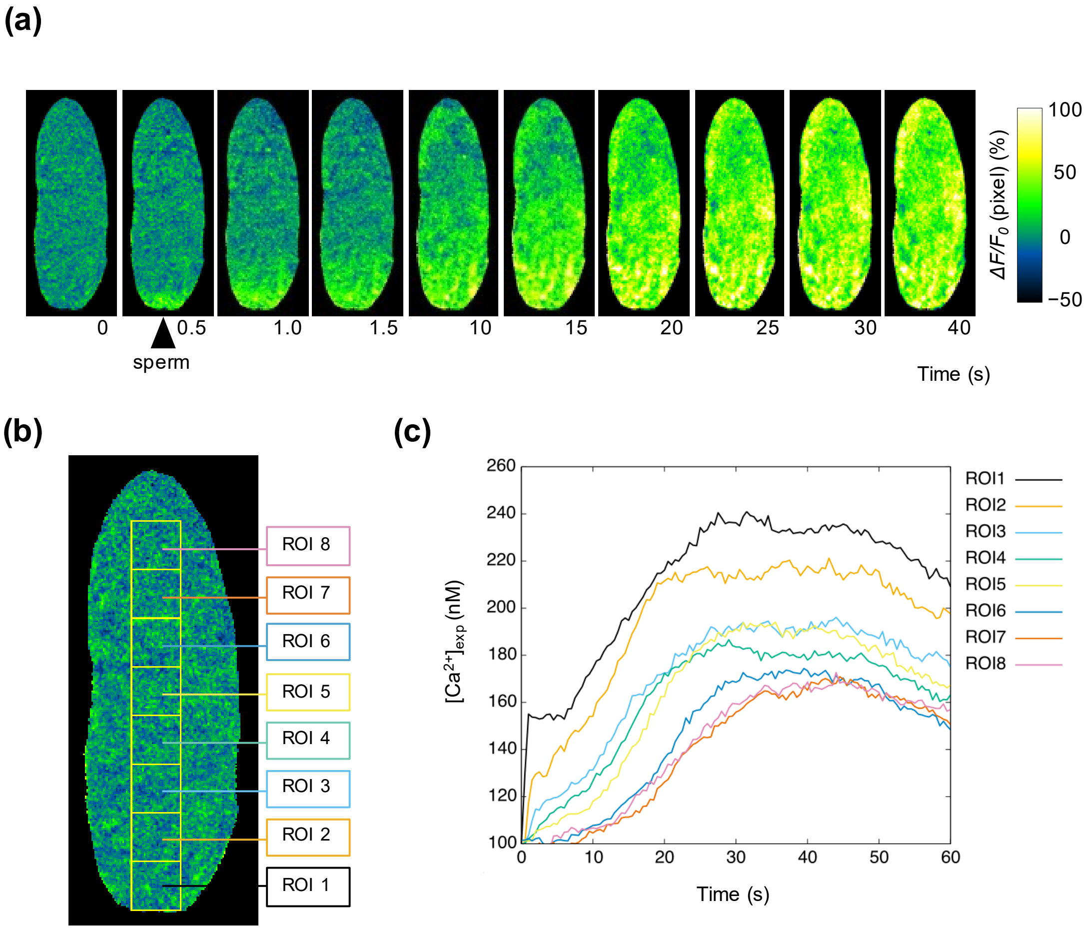

Figure 5.1 Quantification of experimental data.

(a) Time-lapse images of Ca^{2+} wave in a fertilized oocyte of the nematode *Caenorhabditis elegans*. Black arrowhead indicates the point of sperm entry. (b) Regions of interest (ROIs). (c) Quantification of Ca^{2+} dynamics in each ROI.

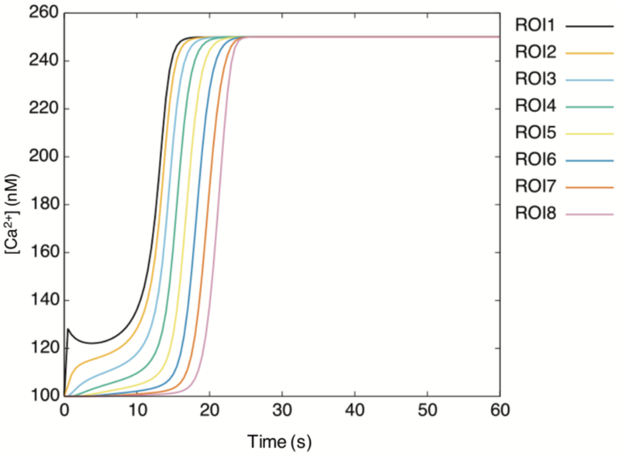

Figure 5.2 Representative results of simulation using the Nagumo model.

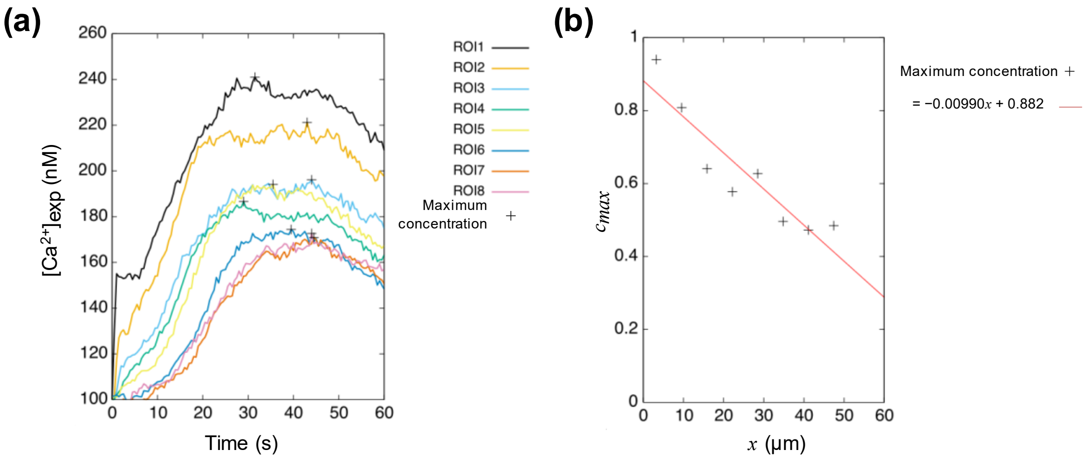

Figure 5.3 Obtaining the c_{max} function.

(a) Ca^{2+} dynamics in each ROI. (b) The c_{max} function. The horizontal axis indicates the distance from the point of sperm entry.

5.2.2 Parameter Search

To examine whether my model can produce a biphasic waveform and the distance-dependent decrease in convergence values, I searched the threshold α ($0 < \alpha < 1$) and amplitude A ($A > 0$). The concentration c was calculated by exhaustively combining the parameters within the following range: $0.025 < \alpha < 1$ and $2.5 < A < 40$ ($\Delta\alpha = 0.025$, $\Delta A = 2.5$). From the distribution of the total absolute error (Figure 5.4), I found that it was smallest in the range $0.005 < \alpha < 0.1$ and $1 < A < 5$. Thus, the range of parameter search for α and A was set as $0.005 < \alpha < 0.1$ for α ($\Delta\alpha = 0.005$) and $0.25 < A < 5$ ($\Delta A = 0.25$).

Parameter spaces for the presence of the biphasic waveform and for the convergence to c_{max} are shown in Figure 5.5a and b, respectively. I found a range that satisfied both conditions (Figure 5.5c). These results showed that my proposed model has a parameter range in which it can produce the biphasic waveform and the distance-dependent decrease in convergence values.

Next, I searched for parameters that minimize total absolute error within the range (Figure 5.5d). The total absolute error was lowest at $\alpha = 0.010$, $A = 1.75$ (Figure 5.5d). Results of simulation with this parameter set was shown in Figure 5.5e. The wave speed with this parameter was about 4.8 µm/s. In experiment, the wave speed was estimated to be about 1.0 µm/s [22]. The wave speed in simulations is the same as that in experiments in the order of magnitude. By searching α and A, my model can produce a waveform qualitatively similar to the observed waveform in that the maximum concentration values decrease with increasing distance from the point of sperm entry, whereas the maximum values are constant in the previous model. I also confirmed that my new model can produce the biphasic waveform simultaneously with the decrease of the maximum concentration.

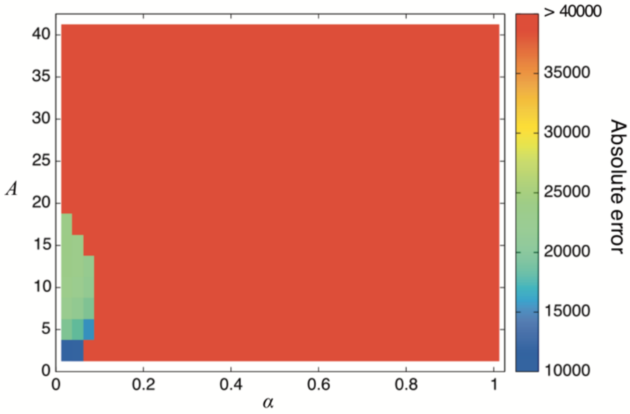

Figure 5.4 Distribution of the total absolute error.

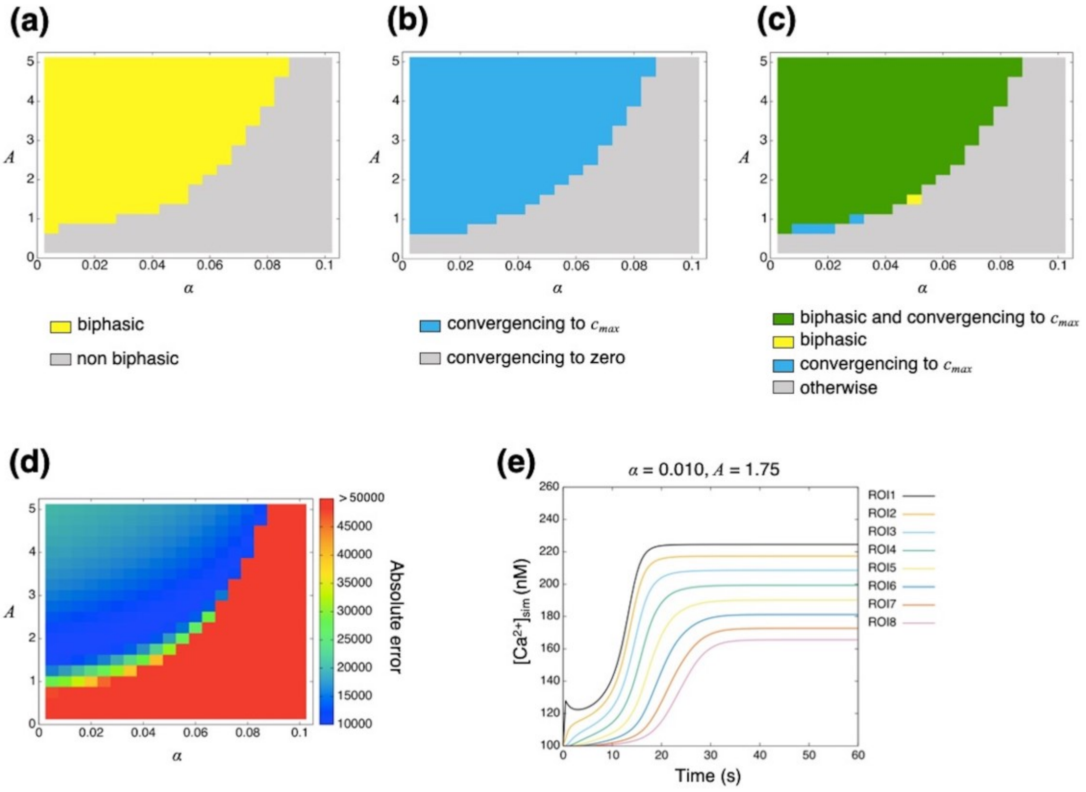

Figure 5.5 Parameter search for biphasicity and convergence.

(a) Parameter space in which my model produces or does not produce the biphasic waveform. (b) Parameter space in which my model produces a wave converging to c_{max} or zero. (c) Parameter spaces in which my model produces a biphasic wave converging to c_{max} (green), only a biphasic waveform (yellow), only a wave converging to c_{max} (blue), and a non-biphasic wave converging to zero (grey). (d) Distribution of total absolute error. (e) Results of simulation at the best parameter combination ($\alpha = 0.010$, $A = 1.75$), which minimizes total absolute error.

To examine whether the best parameter set for one oocyte is consistent among other oocytes, I simulated Ca^{2+} wave in another wild-type oocyte. Three ROIs (15 ×15 pixels each) were set along the long axis of the oocyte (Figure 5.6a) and $[Ca^{2+}]_{exp}$ was calculated for each ROI (Figure 5.6b). The spatial step size was set to 0.42 µm. I simulated Ca^{2+} wave in the second oocyte by using equation (5.3) and (5.4) with the best parameter set for the first oocyte (Figure 5.7). The result showed a biphasic waveform as well as the decrease in the maximum concentration with increasing distance from the point of sperm entry. However, the converged concentrations were markedly different from those in the experimental data.

The converged concentrations in simulation depend on the c_{max} function and the scaling equation. To reduce the differences in the converged concentrations between the simulation and the experiment, I generated a new c_{max} function and a new scaling equation optimized for the second oocyte, as expressed in equation (5.5) and (5.6), respectively.

$$c_{max} = -0.0136\,x + 0.953 \tag{5.5}$$

$$[\mathrm{Ca}^{2+}]_{\mathrm{sim}} = 80\,c + 100 \tag{5.6}$$

To examine whether the model using the new c_{max} function and the new scaling equation can produce a waveform similar to that in the second oocyte, I searched the threshold α ($0.005 < \alpha < 0.1$) and amplitude A ($0.25 < A < 5$). The results of simulation at the parameter combination ($\alpha = 0.035$, $A = 1.25$), which minimized total absolute error, are shown in Figure 5.8a. The results with the best parameter combination for the first oocyte ($\alpha = 0.010$, $A = 1.75$) are also shown (Figure 5.8b). These waveforms are similar to that in the second oocyte in the converged concentration and the wave speed.

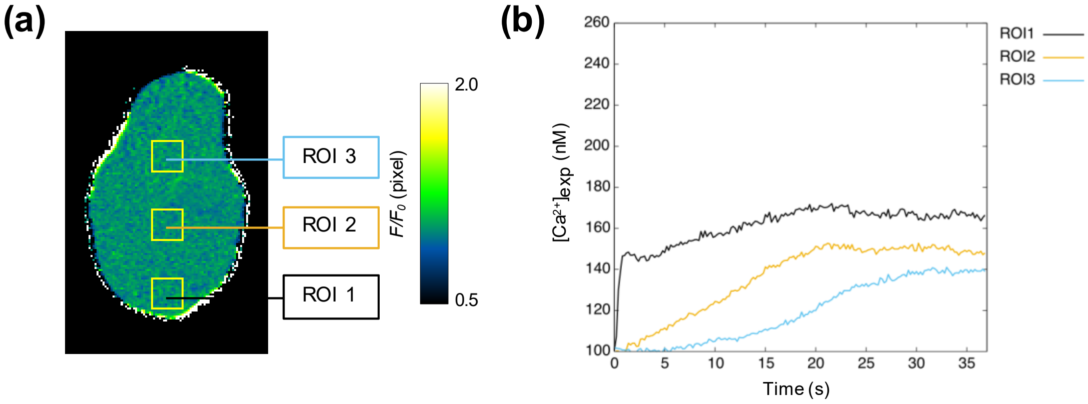

Figure 5.6 Quantification of experimental data of the second oocyte.

(a) Regions of interest (ROIs). (b) Quantification of Ca^{2+} dynamics in each ROI.

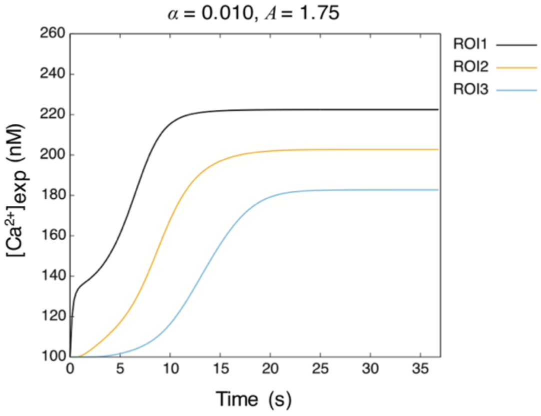

Figure 5.7 Results of simulation of the second oocyte using the c_{max} function and the scaling equation optimized for the first oocyte with the best parameter set for the first oocyte ($\alpha = 0.010$, $A = 1.75$).

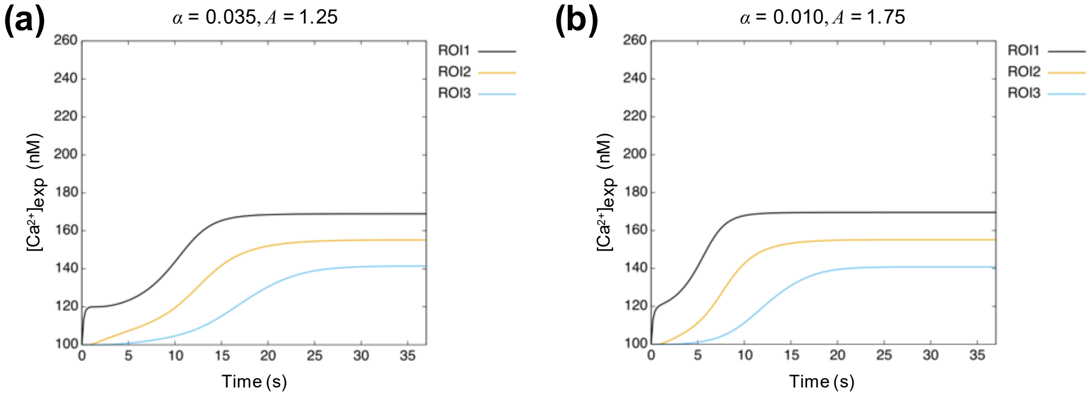

Figure 5.8 Results of the model using the c_{max} function and the scaling equation optimized for the second oocyte.

(a) Results of simulation at the best parameter combination ($\alpha = 0.035$, $A = 1.25$), which minimizes total absolute error.

(b) Results of simulation at the best parameter combination for the first oocyte ($\alpha = 0.010$, $A = 1.75$).

5.3 Discussion

I introduced a linear monotonically decreasing function into the reaction part of the Nagumo model. In the modified model, the convergence values depend on the position in the oocyte. My model qualitatively reproduced the observed decrease in the maximum Ca^{2+} concentration with increasing distance from the point of sperm entry. In my model, I used the linear function c_{max} instead of the constant 1 in the Nagumo model. The proposed model assumes that c_{max}, which can be regarded as the upper limit of the Ca^{2+} concentration at which there is no net flux through Ca^{2+} channels, depends on the distance from the point of sperm entry, whereas the Nagumo model assumes that the limit is the same in different regions of the oocyte. These results might be explained by a non-uniform distribution of Ca^{2+} stores along the long axis of the fertilized oocyte. In fact, the endoplasmic reticulum is not uniformly distributed in the oocyte [112]. Alternatively, a diffusible factor(s) introduced by the sperm may be non-uniformly distributed and thus non-uniformly affect the upper limit Ca^{2+} concentration of the Ca^{2+} channel in the oocyte. In fertilized oocytes of the polyspermic newt, Ca^{2+} wave starting from the sperm entry point does not reach the opposite pole of the oocyte [113]. This phenomenon might be explained by the distribution of a sperm factor only in a small part of the oocyte. Takayama and Onami observed that the maximum Ca^{2+} concentration decreased with increasing distance from the point of sperm entry in a mutant oocyte where the sperm entered from the lateral side of the oocyte [22]. The non-uniformity of sperm factor distribution possibly causes the non-uniform activity of Ca^{2+} channels. A stable linear gradient of sperm factor can be generated by the source-sink mechanism [114]. Alternatively, a transient gradient might be generated by simple diffusion of the sperm factor. Further experiments are needed to clarify the mechanism. A mammalian sperm factor is the sperm-specific phospholipase C ζ [11], which does not have an apparent ortholog in *C. elegans*.

Adjustment of the α and A parameters resulted in a biphasic waveform. Thus, my model can reproduce a clear biphasic waveform and the changes in the convergence values depending on the position in the oocyte.

The c_{max} function and scaling equation optimized for the first oocyte did not produce similar waveform to that in the second oocyte, whereas those optimized for the second oocyte produced similar one even when with the best parameter set for the first oocyte. The results suggest that the basic property of Ca^{2+} channels, relating to parameters α and A, does not differ among oocytes. It is likely that the difference in the waveform among oocytes largely comes from the difference in the spatial distribution of the activity of Ca^{2+} channels.

I must note the remaining inconsistencies between my model and experimental results; for example, Ca^{2+} concentration calculated in my model was constant after it converged, whereas it actually gradually decreases after reaching maximum. My model cannot reproduce this decrease because c increases until it reaches the c_{max}. To overcome this limitation, I may need to further modify the reaction term.

I evaluated the waveform and the convergence values of the simulation results calculated in one dimension. Although such calculations are sufficient for qualitative evaluation of waveform propagation along the long axis of the oocyte, they are insufficient to simulate more complex situations. Three-dimensional calculations may be necessary for a more rigorous simulation. Thus, I need to further improve the model in order to resolve the differences between simulated and experimental results.

5.4 Methods

5.4.1 Calculation and Parameter Settings

The explicit Euler method was used for the reaction term, and the implicit method was used for the diffusion term to solve reaction–diffusion equations. I used the Neumann boundary condition, which assumes that there is no flow in or out of the oocyte. The oocyte was assumed to be a one-dimensional bar 57 μm in length. The diffusion coefficient was set to 20 $\mu m^2/s$ [115]. The initial concentration f_0 was given by equation (5.7), where x is the distance from the point of sperm entry. The spatial step size was 0.21 μm and the time step size was 0.001 s.

$$f_0 = \begin{cases} 7 & (x = 0) \\ 0 & (x \neq 0) \end{cases} \tag{5.7}$$

5.4.2 Quantification

Ca^{2+} concentration in a ROI of the oocyte was calculated by image analysis as described in the reference method [22] (Figure 5.1a). The original image data for Figure 5.1 from the same research group [22] was used for the calculation of the first oocyte. I set eight ROIs (30 × 30 pixels each) along the long axis of the oocyte and numbered them from the point of sperm entry (Figure 5.1b). I quantified the Ca^{2+} fluorescence change relative to that at time zero, $\Delta F/F_0$, for each ROI at each time frame, where $\Delta F = F - F_0$, F is the average fluorescence intensities of all pixels within the ROI, and F_0 is the average fluorescence intensity in each ROI during the initial ten time frames before fertilization (–4.5 s to 0 s). Then I calibrated this fluorescence change to the concentration by equation (5.8) used in the previous study [22] (Figure 5.1c), where $[Ca^{2+}]_{exp}$ is the experimentally determined Ca^{2+} concentration value.

$$[\mathrm{Ca}^{2+}]_{\mathrm{exp}} = 330 \times \frac{4.02\ F/F_0 - 1}{14 - 4.02\ F/F_0} \tag{5.8}$$

Simulated values in the ROIs were calculated by one-dimensional simulation. Because the $[Ca^{2+}]_{exp}$ values ranged from approximately 100 to 250 nM, I scaled the simulated Ca^{2+} concentration values, $[Ca^{2+}]_{sim}$, by equation (5.9) using the concentration variable c of the model. I note that the concentration calculated by equation (5.9) is not necessarily equal to the actual concentration.

$$[\mathrm{Ca}^{2+}]_{\mathrm{sim}} = 150\ c + 100 \tag{5.9}$$

The original image data for Figure S2 in the previous study of the same research group [22] was used for the calculation of the second oocyte. $[Ca^{2+}]_{exp}$ and $[Ca^{2+}]_{sim}$ were calculated as were done for the first oocyte.

5.4.3 Evaluation

(1) Total Absolute Error

Total absolute error E is defined as the sum of the absolute values of the differences between simulated and experimental values in each ROI at each time step. I defined r as the index of the ROIs. Then, E is expressed by equation (5.10) using $[Ca^{2+}]_{sim}(r, t)$ and $[Ca^{2+}]_{exp}(r, t)$.

$$E = \sum_{r=1}^{8} \sum_{t=0}^{60} \left| [\mathrm{Ca}^{2+}]_{\mathrm{sim}}(r,t) - [\mathrm{Ca}^{2+}]_{\mathrm{exp}}(r,t) \right| \tag{5.10}$$

(2) Biphasicity

To evaluate the presence or absence of a biphasic waveform, I used the results for ROI1, in which it appears most clearly. I counted inflection points in the time course of the Ca^{2+} concentration. Two sign changes are observed in the second-order differential values if the biphasic waveform appears, whereas no sign change is observed if it does not appear (Figure 5.9). I judged that the biphasic waveform appears in ROI1 if the number of inflection points was two.

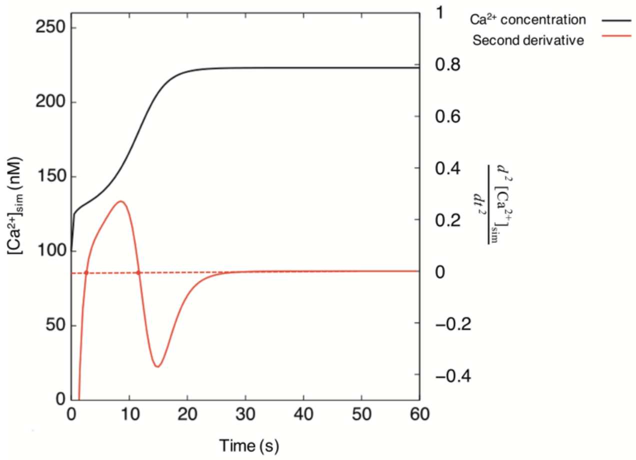

Figure 5.9 An example of a biphasic waveform and the second-order differential values.

(3) Convergence to c_{max}

Simulated values converge to 0 or c_{max} because of the characteristics of the reaction term in my model. I assumed that the simulated values in all ROIs converged when the difference of simulated values of ROI8 between consecutive time steps was less than 0.1 nM continuously for 10 s after 50 s of simlation. I defined the simulated value of ROI8 at the 10 s as the converged concentration. I executed the simulation until ROI8 converged. The converged concentrations obtained in this way were either about 100 nM or about 160 nM. I assumed that the simulated value converged to c_{max} when the converged concentrations were more than 130 nM.

(4) Wave Speed

I calculated $t_{50\%}$, the time when the simulated value exceeded 50% from the initial concentration to the converged concentration, for ROI 2~7. I excluded ROI1 because it showed biphasicity. Then, I calculated Δx and$\Delta t_{50\%}$, the distance and the difference of $t_{50\%}$ between each adjacent ROIs, respectively. The wave speed of simulations was calculated by averagingΔx /$\Delta t_{50\%}$ for all adjacent ROIs.

Chapter 6

Conclusion

6.1 Conclusion

In this study, I aimed to understand the phenomena related to fertilization and developmental ability of oocytes, especially the age-related changes in oocyte quality and the fertilization Ca^{2+} waves. I quantitatively and mathematically analyzed these phenomena using in vivo imaging data of *Caenorhabditis elegans* (*C. elegan*s). I verified whether the quantitative and mathematical analyses provide the biological findings and reasonable hypotheses regarding the phenomena related to fertilization and developmental ability of oocytes.

Firstly, in Chapter 3, I performed statistical image processing of differential interference contrast (DIC) images to quantify the age-associated changes in oocyte appearance, which is thought to reflect oocyte quality. I showed that the cytoplasmic texture significantly changes with aging by using the statistical image features of Max-min Value (Mm Value) and *Correlation* (COR); the Mm Value is the mean difference between the maximum and minimum intensities within each moving window and the Grey Level Co-occurrence Matrix based feature, COR. The analyses using synthetic images suggest that the texture changes characterized by COR reflect increased granule size in the cytoplasm. Manual measurements in the DIC images validated that the cytoplasmic granules in oocytes become larger with aging.

Secondly, in Chapter 4, I predicted the genes involved in reproductive aging by applying the image features proposed in Chapter 3 to the DIC image data obtained from large-scale gene silencing experiments. Genes whose knockdown causes the texture changes as seen in aged oocytes are thought to be candidate genes involved in reproductive aging. These genes were screened by identifying images that had a decreased Mm Value or increased COR – properties that were found to occur in aged oocytes. The cytoplasmic texture images were sourced from the Worm Developmental Dynamics Database 2, which stores DIC microscopy images of early *C. elegans* embryos with genes silenced by RNA interference. Of 316 target genes, five genes (*smc-4*, F10C2.4, *tin-44*, *let-754*, *hmp-2*) were identified to increase Mm Values and one gene (*csr-1*) was identified to increase COR. Of the identified genes, *smc-4* has functions related to chromosome segregation and has been documented to be related to reproductive aging of *C. elegans*. These results suggest that screening Mm Values could identify genes involved in reproductive aging. Through these analyses, six genes were identified to potentially be involved in reproductive aging.

Finally, in Chapter 5, I focused on fertilization Ca^{2+} waves and proposed an improved model based on Nagumo model. In the previous study, reaction-diffusion Nagumo model can produce a similar biphasic waveform to observed one, but cannot represent the observed gradual decrease in maximum Ca^{2+} concentration depending on the position in the oocyte [22]. I introduced a linear monotonically decreasing function into the reaction part of the Nagumo model. I demonstrated that my new model can produce the gradual decrease in maximum Ca^{2+} concentration with increasing distance from the point of sperm entry and a biphasic waveform simultaneously. My model assumed the upper limit of the Ca^{2+} concentration at which there is no net flux through Ca^{2+} channels depends on the distance from the point of sperm entry, which suggests a factor that causes non-uniformity in the amounts of Ca^{2+} released during fertilization.

I quantitatively and mathematically analyzed the age-related changes in oocyte quality and the fertilization Ca^{2+} wave, which are important phenomena related to fertilization and developmental ability of oocytes. I have derived new findings and hypotheses that are potentially useful for understanding the phenomena related to fertilization and developmental ability of oocytes. By image processing of the age-associated changes in the oocyte appearance in the DIC images, I showed that the cytoplasmic texture in oocytes significantly changes with aging. The image analyses using the COR suggest that the size of granules in oocytes increases with aging, which is consistent with the results of manual measurements of granule size in the DIC images. Assuming the DIC granules are yolk granules, the age-associate changes in the cytoplasmic texture might be affected by the amounts of yolk protein in oocytes. In addition, the analyses using the Mm Value in the manipulated images suggest that the contrast of the cytoplasmic texture changes with aging in a spatially inhomogeneous manner. The changes in texture contrast also possibly reflect the biological factor(s) that changes with aging in the oocytes. The candidate genes involved in reproductive aging, which are identified using the image features of Mm Value and COR, included the gene involved in reproductive aging of *C. elegans*. These genes could potentially be involved in reproductive aging. The functions of candidate genes should be verified by biological experiments. The Mm Value and the COR simultaneously changed with aging, whereas the knockdown of specific genes changed the image features independently, suggesting that each of these image features characterizes different properties of the age-associated changes in the cytoplasmic texture. The different properties of age-associated texture changes might be explained by the multiple pathways of reproductive aging. The reproductive aging pathway is possibly associated with the multiple aging pathways, such as the insulin/insulin-like growth factor pathway and the TGF-β Sma/Mab pathway. The model of Ca^{2+} wave proposed in this study suggested a factor that produces a position-dependent gradient of the amounts of Ca^{2+} released. This gradient might be due to the non-uniformity of sperm factor distribution, which might be explained based on sperm factor model, one of the three major models of oocyte activation.

I have performed quantitative image analysis using the oocytes captured by the DIC microscopy and mathematical modeling of Ca^{2+} wave dynamics visualized by high-speed in vivo imaging. I have derived new findings and hypotheses regarding the phenomena of fertilization and developmental ability of oocytes by interpreting the quantitative and mathematical results based on biological mechanisms.

6.2 Future Work

This study is expected to develop fundamental biological research and medical engineering applications. The biological findings and hypotheses derived from this study are expected to be useful for fundamental biological research aimed to elucidate the mechanisms of the phenomena related to fertilization and developmental ability of oocytes. The analysis methods proposed in this study might be applicable to other species as well, which may contribute to the development of assisted reproductive technology (ART) in the medical and animal breeding industries.

The biological findings and hypotheses derived from this study may contribute to elucidate the mechanisms of the age-associated changes in oocyte quality and the fertilization Ca^{2+} waves. The quantitative analysis of age-associated changes in cytoplasmic texture suggests that the size of cytoplasmic granules in oocytes increases with aging. Assuming the granules are yolk granules, biological experiments would enable to verify whether the amounts of yolk protein in oocytes increases with aging. To investigate whether the candidate genes are involved in reproductive aging, which were predicted in this study, gene silencing experiments would enable to confirm whether the genes are involved in reproductive aging. These results will lead to new insights into the age-related changes in oocytes and gene pathways involved in reproductive aging. The model of Ca^{2+} wave may be applicable to aged and mutant oocytes in *C. elegans* and oocytes in other organisms. In this study, I improved the model using Ca^{2+} wave of wild-type *C. elegans*. A study of Ca^{2+} wave of aged or mutant oocytes using the proposed model possibly clarify effects of aging and gene functions on the Ca^{2+} wave. The model of Ca^{2+} wave in *C. elegans* might be applicable to Ca^{2+} waves in other organisms. The model possibly needs to be modified to apply Ca^{2+} waves in other organisms because spatiotemporal patterns of Ca^{2+} response differ among species.

The proposed DIC image features of Mm Value and COR possibly become quantitative markers for clinical observation. The age-related morphological deterioration is a common phenomenon between *C. elegans* and mammals including humans. DIC microscopy, which was used in this study, is often used for observation of oocytes and embryos in ART. Although the various parameters for evaluating human oocyte quality have been proposed, current evaluation methods using the parameters are not able to eliminate subjectivity of observer. The morphological abnormalities in cytoplasmic granules are also found in human oocytes [116]. Proposed image features might be able to characterize the cytoplasmic texture in human oocytes. Further experiments are needed to clarify whether the age-associated changes in cytoplasmic texture can be found in other organisms as seen in *C. elegans*. The image features proposed in my study are expected to contribute to the development of ART in the biomedical, and animal breeding industries.

I hope that this study will contribute to elucidate the mechanisms of phenomena related to the fertilization and development ability of oocytes and will help to develop ART in the biomedical and animal breeding industries.

References

[1] Y. Masui, H. J. Clarke, "Oocyte maturation," *Int. Rev. Cytol.*, vol. 57, pp. 185–282, 1979.

[2] Y. Masui, "From oocyte maturation to the in vitro cell cycle: the history of discoveries of Maturation-Promoting Factor (MPF) and Cytostatic Factor (CSF)," *Differentiation*, vol. 69, pp. 1–17, 2001.

[3] Y. Masui and C. L. Markert, "Cytoplasmic control of nuclear behavior during meiotic maturation of frog oocytes," *J. Exp. Zool.*, vol. 177, pp. 129–145, 1971.

[4] R. B. Gilchrist and J. G. Thompson, "Oocyte maturation: Emerging concepts and technologies to improve developmental potential in vitro," *Theriogenology*, vol. 67, pp. 6–15, 2007.

[5] R. L. Krisher, "The effect of oocyte quality on development," *J. Anim. Sci.*, vol. 82, pp. E14–E23, 2004.

[6] E. R. te Velde and P. L. Pearson, "The variability of female reproductive ageing," *Human Reproduction Update*, vol. 8, pp. 141–154, 2002.

[7] M. Mills, R. R. Rindfuss, P. McDonald, and E. te Velde, "Why do people postpone parenthood? Reasons and social policy incentives," *Human Reproduction Update*, vol. 17, pp. 848–860, 2011.

[8] M. Whitaker, "Calcium at fertilization and in early development," *Physiol. Rev.*, vol. 86, pp. 25–88, 2006.

[9] S. A. Stricker, "Comparative biology of calcium signaling during fertilization and egg activation in animals," *Dev Biols*, vol. 211, pp. 157–176, 1999.

[10] S. Miyazaki *et al.*, "Block of Ca^{2+} wave and Ca^{2+} oscillation by antibody to the inositol 1,4,5-trisphosphate receptor in fertilized hamster eggs," *Science*, vol. 257, pp. 251–255, 1992.

[11] J. Kashir *et al.,* "Comparative biology of sperm factors and fertilization-induced calcium signals across the animal kingdom," *Mol. Reprod. Dev.*, vol. 80, pp. 787–815, 2013.

[12] A. Ajduk, A. Małagocki, and M. Maleszewski, "Cytoplasmic maturation of mammalian oocytes: development of a mechanism responsible for sperm-induced Ca^{2+} oscillations," *Reprod. Biol.*, vol. 8, pp. 3–22, 2008.

[13] J. P. Ozil, *et al.*, "Ca^{2+} oscillatory pattern in fertilized mouse eggs affects gene expression and development to term," *Dev. Biol.*, vol. 300, pp. 534–544, 2006.

[14] J. Carroll, K. Swann, D. Whittingham, and M. Whitaker, “Spatiotemporal dynamics of intracellular [Ca^{2+}]i oscillations during the growth and meiotic maturation of mouse oocytes,” *Development*, vol. 120, pp. 3507–3517, 1994.

[15] K. T. Jones, J. Carroll, and D. G. Whittingham, “Ionomycin, thapsigargin, ryanodine, and sperm induced Ca^{2+} release increase during meiotic maturation of mouse oocytes,” *J. Biol. Chem.*, vol. 270, pp. 6671–6677, 1995.

[16] L. M. Mehlmann and D. Kline, “Regulation of intracellular calcium in the mouse egg: Calcium release in response to sperm or inositol trisphosphate is enhanced after meiotic maturation,” *Biol. Reprod.*, vol. 51, pp. 1088–1098, 1994.

[17] K. Czajkowska *et al.*, “Age-related alterations in fertilization-induced Ca^{2+} oscillations depend on the genetic background of mouse oocytes,” *Biol. Reprod.*, vol. 103, pp. 986–999, 2020.

[18] S. Andux and R. E. Ellis, “Apoptosis maintains oocyte quality in aging *Caenorhabditis elegans* females,” *PLoS Genet.*, vol. 4, e1000295, 2008.

[19] S. Luo, *et al.*, “TGF-β and insulin signaling regulate reproductive aging via oocyte and germline quality maintenance,,” *Cell*, vol. 143, pp. 299–312, 2010.

[20] J. E. Sulston and H. R. Horvitz, “Post-embryonic cell lineage of the nematode, *Caenorhabditis elegans*,” *Dev. Biol.*, vol. 56, pp. 110–156, 1976.

[21] J. E. Sulston, E. Schierenberg, J. G. White, and J. N. Thomson, “The embryonic cell lineage of the nematode *Caenorhabditis elegans*,” *Dev. Biol.*, vol. 100, pp. 64–119, 1983.

[22] J. Takayama and S. Onami, “The sperm TRP-3 channel mediates the onset of a Ca^{2+} wave in the fertilized *C. elegans* oocyte,” *Cell Rep.*, vol. 15, pp. 625–637, 2016.

[23] S. Brenner, “The genetics of *Caenorhabditis elegans*,” *Genetics*, vol. 77, pp. 71–94, 1974.

[24] J. G. White, E. Southgate, J. N. Thomson, and S. Brenner, “The structure of the ventral nerve cord of *Caenorhabditis elegans*,” *Phil. Trans. R. Soc. Lond. B*, vol. 275, pp. 327–348, 1976.

[25] *C. elegans* Sequencing Consortium, “Genome sequence of the nematode *C. elegans*: A platform for investigating biology,” *Science*, vol. 282, pp. 2012–2018, 1998.

[26] A. Fire, *et al.*, “Potent and specific genetic interference by double- stranded RNA in *Caenorhabditis elegans*,” *Nature*, vol. 391, pp. 806–811, 1998.

[27] J. Hodgkin, H. R. Horvitz, and S. Brenner, "Nondisjunction mutants of the nematode *Caenorhabditis elegans*," *Genetics*, vol. 91, pp. 67–94, 1979.

[28] C. Kenyon, "The plasticity of aging: Insights from long-lived mutants," *Cell*, vol. 120, pp. 449–460, 2005.

[29] S. E. Hughes, K. Evason, C. Xiong, and K. Kornfeld, "Genetic and pharmacological factors that influence reproductive aging in nematodes," *PLoS Genet.*, vol. 3, e25, 2007.

[30] S. Luo and C. T. Murphy, "*Caenorhabditis elegans* reproductive aging: Regulation and underlying mechanisms," *Genesis*, vol. 49, pp. 53–65, 2011.

[31] D. Cimadomo, *et al.*, "Impact of maternal age on oocyte and embryo competence," *Front. Endocrinol (Lausanne)*, vol. 29, 327, 2018.

[32] D. Navot *et al.*, "Poor oocyte quality rather than implantation failure as a cause of age-related decline in female fertility," *Lancet*, vol. 337, pp. 1375–1377, 1991.

[33] D.T.Armstrong, "Effects of maternal age on oocyte developmental competence," *Theriogenology*, vol. 55, pp. 1303–1322, 2001.

[34] M. C. Magli, *et al.*, "Embryo morphology and development are dependent on the chromosomal complement," *Fertil. Steril.*, vol. 87, pp. 534–541, 2007.

[35] T. Hassold and P. Hunt, "To err (meiotically) is human: the genesis of human aneuploidy," *Nat. Rev. Genet.*, vol. 2, pp. 280–291, 2001.

[36] F. E. Duncan, *et al.*, "Chromosome cohesion decreases in human eggs with advanced maternal age," *Aging Cell*, vol. 11, pp. 1121–1124, 2012.

[37] Q. Wang and Q.Y. Sun, "Evaluation of oocyte quality: morphological, cellular and molecular predictors," *Reproduction, Fertility and Development*, vol. 19, pp.1–12, 2006.

[38] G. Coticchio, *et al.*, "What criteria for the definition of oocyte quality?," *Ann. N. Y. Acad. Sci.*, vol. 1034, pp. 132–144, 2004.

[39] B. Balaban and B. Urman, "Effect of oocyte morphology on embryo development and implantation," *Reprod. Biomed. Online*, vol. 12, pp. 608–615, 2006.

[40] E. S. Filho, J. A. Noble, and D. Wells, “A review on automatic analysis of human embryo microscope images,” *Open Biomed. Eng. J.*, vol. 4, pp. 170–177, 2010.

[41] P. Khosravi *et al.*, “Deep learning enables robust assessment and selection of human blastocysts after in vitro fertilization,” *NPJ Digit. Med.*, vol. 2, 21, 2019.

[42] C. G. Grupen, M. B. Nottle, and H. Nagashima, “Calcium release at fertilization: Artificially mimicking the oocyte’s response to sperm,” *J. Reprod. Dev.*, vol. 48, pp. 313–333, 2002.

[43] J. Kashir, M. Nomikos, F. A. Lai, and K. Swann, “Sperm-induced Ca^{2+} release during egg activation in mammals,” *Biochem. Biophys. Res. Commun.*, vol. 450, pp. 1204–1211, 2014.

[44] C. M. Saunders *et al.*, “PLCζ: a sperm-specific trigger of Ca^{2+} oscillations in eggs and embryo development,” *Development*, vol. 129, pp. 3533–3544, 2002.

[45] A. A. Tokmakov, *et al.*, “Calcium signaling and meiotic exit at fertilization in *Xenopus* egg,” *Int. J. Mol. Sci.*, vol. 15, pp. 18659–18676, 2014.

[46] L. F. Jaffe, “Calcium explosions as triggers of development,” *Ann. N. Y. Acad. Sci.*, vol. 339, pp. 86–101, 1980.

[47] L. F. Jaffe, “The path of calcium in cytosolic calcium oscillations: a unifying hypothesis,” *Proc. Natl. Acad. Sci. U. S. A.*, vol. 88, pp. 9883–9887, 1991.

[48] K. Swann, “A cytosolic sperm factor stimulates repetitive calcium increases and mimics fertilization in hamster eggs,” *Development*, vol. 110, pp. 1295–1302, 1990.

[49] L. A. Jaffe, “First messengers at fertilization,” *J. Reprod. Fertil. Suppl.*, vol. 42, pp. 107– 116, 1990.

[50] R. M. Schulz and G.S. Kopf, “Molecular basis of mammalian egg activation,” *Curr. Top Dev. Biol.*, vol. 30, pp. 21–62, 1995.

[51] J. P. Evans and G. S. Kopf, “Molecular mechanisms of sperm-egg interactions and egg activation,” *Andrologia*, vol. 30, pp. 297–307, 1998.

[52] J. Wagner, Y. X. Li, J. Pearson, and J. Keizer, “Simulation of the fertilization Ca^{2+} wave in *Xenopus* laevis eggs,” *Biophys. J.*, vol. 75, pp. 2088–2097, 1998.

[53] A. Bugrim, *et al.*, “Sperm initiate a Ca^{2+} wave in frog eggs that is more similar to Ca^{2+} waves initiated by IP3 than by Ca^{2+},” *Biophys. J.*, vol. 84, p. 1580–1590, 2003.

[54] M. R. Klass, “A method for the isolation of longevity mutants in the nematode *Caenorhabditis elegans* and initial results,” *Mech. Ageing Dev.*, vol. 22, pp. 279–286, 1983.

[55] D. B. Friedman and E. T. Johnson, “A mutation in the age-1 gene in *Caenorhabditis elegans* lengthens life and reduces hermaphrodite fertility,” *Genetics*, vol. 118, pp. 75-86., 1988.

[56] C. Kenyon, “A *C.elegans* mutant that lives twice as long as wild type,” *Nature*, vol. 366, pp. 461–464, 1993.

[57] M. R. Klass, “Aging in the nematode *Caenorhabditis elegans*: Major biological and environmental factors influencing life span,” *Mech. Ageing Dev.*, vol. 6, pp. 413–429, 1977.

[58] A. R. Mendenhall, M. G. LeBlanc, D. P. Mohan, and P. A. Padilla, “Reduction in ovulation or male sex phenotype increases long-term anoxia survival in a daf-16-independent manner in *Caenorhabditis elegans*,” *Physiol. Genomics*, vol. 36, pp. 167–178, 2009.

[59] C. Ortiz De Solórzano, *et al.*, “Applications of quantitative digital image analysis to breast cancer research,” *Microsc. Res. Tech.*, vol. 59, pp. 119–127, 2002.

[60] D. Glotsos, *et al.*, “An image-analysis system based on support vector machines for automatic grade diagnosis of brain-tumour astrocytomas in clinical routine,” *Med. Inform. Internet Med.*, vol. 30, pp. 179–193, 2005.

[61] G. A. Losa and C. Castelli, “Nuclear patterns of human breast cancer cells during apoptosis: characterisation by fractal dimension and co-occurrence matrix statistics,” *Cell Tissue Res.*, vol. 322, pp. 257–267, 2005.

[62] M. Masseroli, A. Bollea, and G. Forloni, “Quantitative morphology and shape classification of neurons by computerized image analysis,” *Comput. Methods Programs Biomed.*, vol. 41, pp. 89–99, 1993.

[63] S. Chen, *et al.*, “Recent advances in morphological cell image analysis,” *Comput. Math. Methods Med.*, vol. 2012, 101536, 2012.

[64] P. L. Smitha, L. Shaji, and M. G. Mini, “A review of medical image classification techniques,” *in Proc. Int. Conf. VLSI, Commun. Intrumrnataiom*, pp. 34–38, 2011.

[65] C. Angermueller, T. Pärnamaa, L. Parts, and O. Stegle, “Deep learning for computational biology,” *Mol. Syst. Biol.*, vol. 12, pp. 878, 2016.

[66] R. M. Haralick, K. Shanmugam, and I. Dinstein, “Textural features for image classification,” *IEEE Trans. Syst. Man Cybern.*, vol. SMC-3, pp. 610–621, 1973.

[67] D. M. U. Sabino, L. da Fontoura Costa, E. G. Rizzatti, and M. A. Zago, “A texture approach to leukocyte recognition,” *Real-Time Imaging*, vol. 10, pp. 205–216, 2004.

[68] G. Castellano, L. Bonilha, L. M. Li, and F. Cendes, “Texture analysis of medical images,” *Clin. Radiol.*, vol. 59, pp. 1061–1069, 2004.

[69] N. Zulpe and V. Pawar, “GLCM textural features for Brain Tumor Classification,” *Int. J. Comput. Sci. Issues*, vol. 9, pp. 354–359, 2012.

[70] C. Preza, D. L. Snyder, and J. A. Conchello, “Theoretical development and experimental evaluation of imaging models for differential-interference-contrast microscopy,” *J. Opt. Soc. Am. A, Opt. Image Sci. Vis.*, vol. 16, pp. 2185–2199, 1999.

[71] R. J. Cheeks, *et al.*, “*C. elegans* PAR proteins function by mobilizing and stabilizing asymmetrically localized protein complexes,” *Curr. Biol.*, vol. 14, pp. 851–862, 2004.

[72] K. J. Verbrugghe and R. C. Chan, “Imaging *C. elegans* embryos using an epifluorescent microscope and open source software,” *J. Vis. Exp.*, vol. 2625, 2011.

[73] W. J. Sharrock, *et al.*, “Two distinct yolk lipoprotein complexes from *Caenorhabditis elegans*,” *J. Biol. Chem.*, vol. 265, pp. 14422–14431, 1990.

[74] J. Kimble and W. J. Sharrock, “Tissue-specific synthesis of yolk proteins in *Caenorhabditis elegans*,” *Dev. Biol.*, vol. 96, pp. 189–196, 1983.

[75] B. Grant and D. Hirsh, “Receptor-mediated endocytosis in the *Caenorhabditis elegans* oocyte,” *Mol. Biol. Cell*, vol. 10, pp. 4311–4326, 1999.

[76] D. Garigan, *et al.*, “Genetic analysis of tissue aging in *Caenorhabditis elegans*: a role for heat-shock factor and bacterial proliferation,” *Genetics*, vol. 161, pp. 1101–1112, 2002.

[77] L. A. Herndon *et al.*, “Stochastic and genetic factors influence tissue-specific decline in ageing *C. elegans*,” *Nature*, vol. 419, pp. 808–814, 2002.

[78] M. Perez, M. Francesconi, C. Hidalgo-Carcedo, and B. Lehner, “Maternal age generates phenotypic variation in *Caenorhabditis elegans*,” *Nature*, vol. 552, pp. 106–109, 2017.

[79] D. Gems and Y. de La Guardia, "Alternative perspectives on aging in *Caenorhabditis elegans*: Reactive oxygen species or hyperfunction?," *Antioxid. Redox Signal.*, vol. 19, pp. 321–329, 2013.

[80] C. T. Murphy *et al.*, "Genes that act downstream of DAF-16 to influence the lifespan of *Caenorhabditis elegans*," *Nature*, vol. 424, pp. 277–284, 2003.

[81] N. E. Seah *et al.*, "Autophagy-mediated longevity is modulated by lipoprotein biogenesis," *Autophagy*, vol. 12, pp. 261–272, 2016.

[82] E. Kim, L. Sun, C. V. Gabel, and C. Fang-Yen, "Long-term imaging of *Caenorhabditis elegans* using nanoparticle-mediated immobilization," *PLoS One*, vol. 8, e53419, 2013.

[83] A. D. Samuel, V. N. Murthy, and M. O. Hengartner, "Calcium dynamics during fertilization in *C. elegans*," *BMC Dev. Biol.*, vol. 1, 8, 2001.

[84] D. A. Clausi and M. Jernigan, "A fast method to determine co-occurrence texture features," *IEEE Trans. Geosci. Remote Sens.*, vol. 36, pp. 298–300, 1998.

[85] M. Imakubo, J. Takayama, H. Okada, and S. Onami, "Statistical image processing quantifies the changes in cytoplasmic texture associated with aging in *Caenorhabditis elegans* oocytes," *BMC Bioinformatics*, vol. 22, 73, 2021.

[86] K. Kyoda *et al.*, "WDDD: Worm developmental dynamics database," *Nucleic Acids Research*, vol. 41, pp. D732–D737, 2013.

[87] R. Kamath *et al.*, "Systematic functional analysis of the *Caenorhabditis elegans* genome using RNAi," *Nature*, vol. 421, pp. 231–237, 2003.

[88] C. Conrad and D. W. Gerlich, "Automated microscopy for high-content RNAi screening," *J. Cell Biol.*, vol. 22, pp. 453–461, 2010.

[89] S. E. Mohr and N. Perrimon, "RNAi screening: new approaches, understandings and organisms," *WIREs RNA*, vol. 3, pp. 145–158, 2012.

[90] K. A. Hagstrom, V. F. Holmes, N. R. Cozzarelli, and B. J. Meyer, "*C. elegans* condensin promotes mitotic chromosome architecture, centromere organization, and sister chromatid segregation during mitosis and meiosis," *Genes Dev.*, vol. 16, pp. 729–742, 2002.

[91] S. Luo, W. M. Shaw, J. Ashraf, and C. T. Murphy, “TGF-ß Sma/Mab signaling mutations uncouple reproductive aging from somatic aging,” *PLoS Genet.*, vol. 5, e1000789, 2009.

[92] T. Hamatani *et al.*, “Age-associated alteration of gene expression patterns in mouse oocytes,” *Human Molecular Genetics*, vol. 13, pp. 2263–2278, 2004.

[93] N. M. Steuerwald, M. G. Bermúdez, D. Wells, S. Munné, and J. Cohen, “Maternal age-related differential global expression profiles observed in human oocytes,” *Reprod. Biomed. Online*, vol. 14, pp. 700–708, 2007.

[94] S. E. Encalada *et al.*, “DNA replication defects delay cell division and disrupt cell polarity in early *Caenorhabditis elegans* embryos,” *Dev. Biol.*, vol. 228, pp. 225–238, 2000.

[95] W. Neupert and J. M. Herrmann, “Translocation of proteins into mitochondria,” *Annual Review of Biochemistry*, vol. 76, pp. 723–749, 2007.

[96] D. Mokranjac and W. Neupert, “The many faces of the mitochondrial TIM23 complex,” *Biochim. Biophys. Acta. Bioenerg.*, vol. 1797, pp. 1045–1054, 2010.

[97] A. Dillin, D. K. Crawford, and C. Kenyon, “Timing requirements for insulin/IGF-1 signaling in *C. elegans*,” *Science.*, vol. 298, pp. 830–834, 2002.

[98] C. Bennett *et al.*, “Activation of the mitochondrial unfolded protein response does not predict longevity in *Caenorhabditis elegans*,” *Nat. Commun.*, vol. 5, 3483, 2014.

[99] M. R. Jones, *et al.*, “Oligonucleotide Array Comparative Genomic Hybridization (oaCGH) based characterization of genetic deficiencies as an aid to gene mapping in *Caenorhabditis elegans*,” *BMC Genomics*, vol. 8, 402, 2007.

[100] H. Stewart *et al.*, “Lethal mutations defining 112 complementation groups in a 4.5 Mb sequenced region of *Caenorhabditis elegans* chromosome III,” *Mol. Gen. Genet. MGG*, vol. 260,pp. 280–288, 1998.

[101] M. Costa, *et al,*, “A putative catenin-cadherin system mediates morphogenesis of the *Caenorhabditis elegans* embryo,” *J. Cell Biol.*, vol. 141, pp. 297–308, 1998.

[102] D. Warde-Farley *et al.*, “The GeneMANIA prediction server: biological network integration for gene prioritization and predicting gene function,” *Nucleic Acids Research*, vol. 38, pp. 214–220, 2010.

[103] F. Piano *et al.*, “Gene clustering based on RNAi phenotypes of ovary-enriched genes in *C. elegans*,” *Curr. Biol.*, vol. 12, pp. 1959–1964, 2002.

[104] K. C. Gunsalus, W. C. Yueh, P. MacMenamin, and F. Piano, "RNAiDB and PhenoBlast: web tools for genome-wide phenotypic mapping projects," *Nucleic Acids Research*, vol. 32, pp. D406–D410, 2004.

[105] E. Yigit *et al.*, "Analysis of the *C. elegans* Argonaute family reveals that distinct Argonautes act sequentially during RNAi," *Cell*, vol. 127, pp. 747–757, 2006.

[106] A. C. Campbell and D. L. Updike, "CSR-1 and P granules suppress sperm-specific transcription in the *C. elegans* germline," *Development*, vol. 142, pp. 1745–1755, 2015.

[107] R. R. Zwaal, *et al.*, "G proteins are required for spatial orientation of early cell cleavages in *C. elegans* embryos," *Cell*, vol. 86, pp. 619–629, 1996.

[108] M. Gotta and J. Ahringer, "Distinct roles for Gα and Gβγ in regulating spindle position and orientation in *Caenorhabditis elegans* embryos," *Nat. Cell Biol.*, vol. 3, pp. 297–300, 2001.

[109] C. Kenyon, "The first long-lived mutants: discovery of the insulin/IGF-1 pathway for ageing," *Phil. Trans. R. Soc. B,* vol. 366, pp. 9–16, 2011.

[110] S. Hamahashi, S. Onami, and H. Kitano, "Detection of nuclei in 4D Nomarski DIC microscope images of early *Caenorhabditis elegans* embryos using local image entropy and object tracking," *BMC Bioinformatics*, vol. 6, 125, 2005.

[111] B. Zinner, "Existence of traveling wavefront solutions for the discrete Nagumo equation," *Journal of Differential Equations*, vol. 96, pp. 1–27, 1992.

[112] D. Poteryaev *et al.*, "Involvement of the actin cytoskeleton and homotypic membrane fusion in ER dynamics in *Caenorhabditis elegans*," *Mol. Biol. Cell*, vol. 16, pp. 2139–2153, 2005.

[113] Y. Iwao, "Egg activation in physiological polyspermy," *Reproduction*, vol. 144, pp. 11–22, 2012.

[114] F. Crick, "Diffusion in embryogenesis," *Nature*, vol. 225, p. 420–422 , 1970.

[115] N. L. Allbritton, T. Meyer, and L. Stryer, "Range of messenger action of calcium ion and inositol 1,4,5-trisphosphate," *Science*, vol. 258, pp. 1812–1815, 1992.

[116] L. Rienzi, G. Vajta, and F. Ubaldi, "Predictive value of oocyte morphology in human IVF: a systematic review of the literature," *Human Reproduction Update*, vol. 17, pp. 34–45, 2011.

Research Achievements

Publication

M. Imakubo, J. Takayama, H. Okada, and S. Onami. “Statistical image processing quantifies the changes in cytoplasmic texture associated with aging in *Caenorhabditis elegans* oocytes,” *BMC Bioinformatics*, vol. 22, 73, 2021.

M. Imakubo, K. Kyoda, H. Itoga,, J. Takayama, and S. Onami, “Texture-based Screening to Identify Genes Involved in Reproductive Aging in *Caenorhabditis elegans*,” *Journal of Image and Graphics* (accepted).

M. Imakubo, J. Takayama, and S. Onami, “Improvement and Evaluation of a Mathematical Model for Fertilization Calcium Waves in *Caenorhabditis Elegans*,” *IPSJ Transactions on Bioinformatics*, vol. 11, pp. 24–30, 2018.

International conference

(oral) Momoko Imakubo, Koji Kyoda, Hiroya Itoga, Jun Takayama, Shuichi Onami “Texture-based Screening to Identify Genes Involved in Reproductive Aging in *Caenorhabditis elegans*” 2020 2nd Asia Digital Image Processing Conference, 2020.12.4

Domestic conference

(oral) 今久保 桃子，高山 順，大浪 修一 「線虫 *Caenorhabditis elegans* の受精カルシウム波の数理モデルの改良と評価」第 118 回 MPS・第 54 回 BIO 合同研究発表会， 2018.6.15

Acknowledgements

I would like to express my sincere appreciation to my academic advisor, Professor Shuichi Onami for giving me the opportunity to work on this project and for his guidance and encouragement through the learning process of my study. I would like to express my gratitude to Professor Zhiwei Luo, Professor Takenao Ohkawa, and Professor Shigenori Tanaka for their valuable advices in the review process.

I would like to express my special gratitude to Dr. Jun Takayama for the kind instruction and meaningful discussion throughout all experiments. I would like to express my gratitude to Dr. Koji Kyoda for the valuable advice and helpful suggestions on my study. I would like to express my gratitude to Ms. Hatsumi Okada for biological experiments and technical supports. I would like to express my gratitude to Dr. Hiroya Itoga for assistance with the management of database. I would like to thank all members in the Onami laboratory for their helpful suggestions on my study. I am also grateful to my colleagues in Sysmex Corporation for their encouragement.

Finally, I would like to thank my parents, Tadahiro and Mami, and my brother, Tetsuya for their tireless encouragement, support and understanding throughout the years.

Doctor Thesis, Kobe University

“Quantitative analysis of the oocyte quality changes and the fertilization Ca^{2+} wave in *C. elegans*”, 69 pages

Submitted on January, 16, 2021

The date of publication is printed in cover of repository version published in Kobe University Repository Kernel.

© Momoko Imakubo

All Right Reserved, 2021